# A new divergence-free synthetic eddy method for generating homogeneous isotropic turbulence with a prescribed energy spectrum

Yunzhu Cai[a], Jiawei Wan[b,c,*], Ahsan Kareem[b]

[a] *College of Civil Engineering, Nanjing Tech University, China*
[b] *Nathaz Modeling Laboratory, University of Notre Dame, United States*
[c] *China Energy Science and Technology Research Institute Co. Ltd., China*

**Abstract**

A new divergence-free synthetic eddy method (SEM) for the generation of homogeneous isotropic turbulence (HIT) with a prescribed energy spectrum is presented. In the proposed method, the divergence-free consistent synthetic velocity field is generated from the curl of a vector potential field following conventional SEM methodology. A carefully designed formula is constructed for the computation of the local vector potential field induced by each synthetic eddy, with which a desired velocity spectrum tensor can be satisfied for the synthetic incompressible turbulence exactly. The proposed method is characterized by a multi-scale feature in which the length scales of synthetic eddies are determined by a dimensionless random variable satisfying a particular probability distribution function (PDF). The mathematical relation, concerning the energy spectrum of the synthetic turbulence, the shape function of the eddies and the PDF of the eddy-scale-related random variable, is derived. This assists in determining either the shape function or the PDF. The performance of the proposed method is examined by synthesizing HIT satisfying a theoretical energy spectrum model and HIT identified in a wind-tunnel experiment.

*Keywords:* homogeneous isotropic turbulence, synthetic eddy method, divergence-free, energy spectrum, multi-scale

## 1. Introduction

In computational wind engineering, the generation of synthetic turbulence with prescribed statistical properties is of great importance in many applications. Research activities on this topic have been vigorous over the past decades and have branched out into several categories of techniques. Among these, a technique known in the literature either as the synthetic eddy method (SEM) [1] or the turbulent spot method (TSM) [2], has been drawing increasing attention in recent years. This technique attempts to model the real turbulence as a superposition of coherent structures which are randomly placed in space. These coherent structures are referred to as eddies and spots in the SEM and TSM, respectively. Each coherent structure carries an inner velocity distribution determined by the so-called shape function of the eddy (or the spot). The shape function takes a non-dimensional local coordinate, measuring the distance of a spatial coordinate to an eddy center in relative to the dimension of the eddy, as the input variable. A single or multiple length scales are assigned to each eddy to quantity its dimension, which are closely related to the integral length scales of the synthetic turbulence. The velocity distribution resulting from the shape function will be multiplied by some scaling factors before adding it up to the final synthetic turbulence. These scaling factors can be divided into two parts in which one controls the Reynolds stresses of the synthetic turbulence and the other adds randomness to the sign of velocity fluctuations. The former part is usually referred to as the intensity or strength of the eddy.

* Corresponding author
*Email addresses:* yunzhucai@njtech.edu.cn (Yunzhu Cai), jwan1@nd.edu (Jiawei Wan), kareem@nd.edu (Ahsan Kareem)

Ever since the early development of the SEM or TSM, continued efforts have been made to refine this scheme, with the aim of making the synthetic turbulence more closer to the real one, from the statistical point of view. In the original SEM developed by [1], the three velocity components are first generated as independent random variables with an unit variance and then multiplied with a Lund transformation matrix to acquire the desired magnitudes. Efficient as it is in reproducing Reynolds stresses with arbitrary anisotropy, the Lund transformation however destroys the continuity of the original synthetic velocity (if present). Moreover, only a single length scale is assigned to each eddy in [1] such that the multiple length scales of turbulence cannot be reproduced. The random spot method proposed by [2] is almost identical to the SEM by [1] except that there are three length scales assigned to each eddy. By doing so, the integral length scale of each synthetic velocity component in its own direction can be managed to meet with a prescribed value. The work of [2] also suggests that, by representing the shape function as a basic function (such as the polynomial representation) with some unknown coefficients, it is possible to synthesize turbulence satisfying the prescribed autocorrelation functions. The author of [1] later came up with a modified SEM (see chapter 7 of [3]) in which a total of nine length scales are assigned to each eddy such that the integral length scales of each synthetic velocity component in three orthogonal directions can be adjusted according to interest.

Experience shows that violation of the divergence-free constraint in synthetic turbulence can be a disturbing issue for numerical simulations, due to the coupling between the velocity and pressure in the governing equations of fluid flows. It usually results in strong disturbances of the pressure field which in turn alter the velocity field, deviating the statistical properties of the turbulent velocity from the prescribed ones. This leads to the development of synthetic methods satisfying the divergence-free constraint. As a basic approach employed by most of the studies on this issue, a divergence-free velocity field can be obtained by first synthesizing a vector potential field (similar to the way velocity fields are generated in the aforementioned SEM and TSM) and then taking its curl. Although this approach of enforcing the divergence-fee constraint is universal, the way how the vector potential is computed differs from method to method.

In the early work of [4], the vector potential carried by each eddy is taken as the product of a scalar field and a random orientation vector, in which the scalar field is described by a shape function (identical for all eddies) determined from a prescribed energy spectrum. If the orientation vector is uniformly distributed on a sphere, the velocity field resulting from the synthetic eddies will be isotropic. Otherwise, the synthetic turbulence will be anisotropic in Reynolds stresses. However, only a weak level of anisotropy can be reproduced through the spherical asymmetry of the orientation vector. The method later developed by [5] specifies the vector potential as the vorticity of the velocity and employs three length scales (one in each axial direction) to quantify the size of eddies. However, the three length scales (or more specifically the ratios between them) introduced in [5] are determined according to the anisotropy of the prescribed Reynolds stresses rather than the desired integral length scales of the synthetic turbulence. For the generation of turbulence with arbitrary anisotropy in both Reynolds stresses and integral length scales, [6] developed a divergence-free method where the vector potential carried by each eddy is computed with a particular shape function parameterized by three length scales and three intensities of the eddy. These six parameters are designed to fulfill the integral length scale of each velocity component in its own direction, in addition to the prescribed Reynolds stresses. However, only two of the three desired length scales can be exactly satisfied due to the constraint resulting from the shape function employed in [6]. The study of [7] considered a more general approach for the computation of the vector potential in which each individual component of the vector potential can be computed with a shape function and a length scale different from those of the other two components. This feature gives the method of [7] the ability of tackling the issue encountered in the method of [6] concerning the anisotropy in integral length scales.

As a one step further to the fulfillment of the Reynolds stresses and integral length scales, the generation of divergence-free turbulence satisfying some prescribed velocity spectra (or correlation functions) turns out to be a very challenging issue in SEM, especially when compared with Fourier-based synthetic methods such as [8, 9, 10]. In addition to the approach of determining the shape function according to related velocity spectra as the way [2] suggests, another technique employed in [11, 12] that has shown its effectiveness concerning this issue is the use of multi-scale eddies. When synthetic eddies are assigned to different scales or different sets of scales, the velocity spectrum of the turbulence resulting from these multi-scale eddies can be considered as a weighted average of the velocity spectra of the turbulence generated by eddies of each scale. By adjusting the probability and intensity parameters of the multi-scale eddies, the velocity spectrum of the synthetic turbulence can be sought to

match with the prescribed one. The idea behind this technique is consistent with the fact that turbulence is a flow regime characterized by vorticity fluctuations with a broad range of time and length scales. In the work of [12], a multi-scale method based on the modified SEM by [3] is developed where all synthetic eddies are divided into a limited number of eddy groups. The eddies in each group is assigned to a set of parameters which control the length scales and intensities of the eddies in this group. As the number of the parameters grows linearly with the number of the eddy groups, a sophisticated fitting algorithm is presented in [12] for the determination of all unknown parameters. Again, due to the use of the Lund transformation, the turbulence obtained from the method of [12] is not divergence-free. Another attempt made by [11] applies the divergence-free SEM of [7] to the generation of homogeneous isotropic turbulence (HIT) satisfying the von Kármán velocity spectra. To achieve this goal, each synthetic eddy is assigned to three length scales and three intensity parameters, all of which are generated as independent random variables following uniform distributions. The lower and upper limits of the scales and intensities of the eddies are optimized by minimizing the difference between the spectra of the synthetic turbulence and the prescribed ones.

After the discussion on the state-of-art of the SEM and TSM, readers may find that we are particularly concerned with the length scales used to quantify the size of the eddy. This is mainly because the number of length scales assigned to each eddy and how they are employed in the computation of the shape function directly affect the capability of a synthetic method in meeting with the conditions related to the integral length scales. It is noted that most studies concerning divergence-free methods did not present any explicit relations between the length scales of the eddy and those of the synthetic turbulence, except [6]. Considering the limitations existing in the methods mentioned above, the aim of this study is to improve the ability of the SEM methodology in reproducing prescribed Reynolds stresses, integral length scales and velocity spectra without violating the divergence-free constraint.

As a first step to achieve this goal, this study only concerns the generation of HIT. In the proposed method, the divergence-free constraint is enforced by computing the turbulent velocity field as the curl of a vector potential field following conventional methodology. Each synthetic eddy is assigned to a single length scale which varies from eddy to eddy. The vector potential carried by each eddy is computed from a shape function which takes the non-directional relative distance from a spatial location to the center of the eddy as its argument. It will be verified that this treatment is sufficient and vital for the synthetic turbulence to satisfy all related second-order statistics of HIT. The major difference between the multi-scale feature in the proposed method and the techniques of [11, 12] is that the length scales of the eddies are now determined by a dimensionless random variable satisfying a particular probability density function (PDF). By investigating its relationship with the energy spectrum of the synthetic turbulence and the shape function of the eddies, the determination of the PDF of the eddy-scale-related random variable is discussed in detail. The multi-scale technique in the proposed method can be easily extended to the SEM methodology (e.g., [3, 6]) for anisotropic turbulence by making the anisotropic length scale set of eddies dependent on the introduced random variable.

The structure of this paper is organized as follows. Section 2 introduce the proposed synthetic eddy method in which a majority of the content is spent on the second-order statistics of the synthetic turbulence. Some numerical issues concerning the application of the proposed method in practice are discussed in section 3. Section 4 demonstrates the application of the proposed method to the generation of HIT confirming to a particular energy spectrum. An additional numerical example is presented in section 5 to further examine the performance of the proposed method. Concluding remarks are finally presented in section 6.

## 2. A new divergence-free synthetic eddy method

### *2.1. A brief review of the second-order statistics of HIT*

The energy spectrum tensor of incompressible HIT, according to [13], admits the form of

$$\Phi_{ij}(\boldsymbol{\kappa}) = \frac{E(\kappa)}{4\pi\kappa^4}\left(\kappa^2\delta_{ij} - \kappa_i\kappa_j\right), \tag{2.1}$$

where $\boldsymbol{\kappa} = (\kappa_1, \kappa_2, \kappa_3)$ is the vector of wavenumbers, $\kappa = (\kappa_1^2 + \kappa_2^2 + \kappa_3^2)^{1/2}$ is the magnitude of $\boldsymbol{\kappa}$ and $E(\kappa)$ is the so-called energy spectrum function. Meanwhile, the Reynolds stress tensor $\tau_{ij}$ of turbulence can be obtained by

integrating $\Phi_{ij}(\boldsymbol{\kappa})$ over all $\boldsymbol{\kappa}$-space, i.e.,

$$\tau_{ij} = \langle u_i u_j \rangle = \iiint_{-\infty}^{\infty} \Phi_{ij}(\boldsymbol{\kappa})\, \mathrm{d}\boldsymbol{\kappa}. \tag{2.2}$$

Inserting eq. (2.1) into eq. (2.2), we have the Reynolds stress tensor of incompressible HIT satisfy

$$\tau_{ij} = \begin{cases} \tau & i = j, \\ 0 & i \neq j, \end{cases} \quad \tau = \frac{2}{3}\int_0^{\infty} E(\kappa)\, \mathrm{d}\kappa. \tag{2.3}$$

The integral length scale of the $i$-component velocity in the $x_j$-direction (denoted by $L_{ii}^{(j)}$ in the following context), defined as

$$L_{ii}^{(j)} = \frac{1}{\tau_{ii}} \int_0^{\infty} R_{ii}(\boldsymbol{e}_j r)\, \mathrm{d}r, \tag{2.4}$$

where $R_{ij}$ is the velocity correlation tensor, $\boldsymbol{e}_j$ stands for an unit vector in the $x_j$-direction, can be shown to satisfy for incompressible HIT the relation

$$L_{ii}^{(j)} = \begin{cases} l & i = j, \\ l/2 & i \neq j, \end{cases} \quad l = \frac{\pi}{2\tau}\int_0^{\infty} \frac{E(\kappa)}{\kappa}\, \mathrm{d}\kappa. \tag{2.5}$$

*2.2. Formulation of the proposed method*

The discrete locations at which a synthetic turbulence to be generated are basically a finite set of points $S = \{\boldsymbol{x}_1, \ldots, \boldsymbol{x}_s\}$ in space. For the generation of a homogeneous isotropic turbulent velocity field $\boldsymbol{U}(\boldsymbol{x})$ on the point set $S$, the proposed multi-scale synthetic eddy method first synthesizes a total of $N$ eddies surrounding $S$ randomly. Each eddy carries a divergence-free velocity field and is assigned to a unique length scale parameter $\sigma$ characterizing the size of the eddy. The scale $\sigma$ is obtained by multiplying a characteristic length scale $L$ with an independent random variable $\lambda \in [\lambda_{\min}, \lambda_{\max}]$, i.e.,

$$\sigma = \lambda L, \tag{2.6}$$

where $\lambda_{\min}$ and $\lambda_{\max}$ are the lower and upper bounds of $\lambda$, respectively. The random variable $\lambda$ has a prescribed probability distribution $p(\lambda)$ satisfying the normalization

$$\int_{\lambda_{\min}}^{\lambda_{\max}} p(\lambda)\, \mathrm{d}\lambda = 1. \tag{2.7}$$

Note that $L$ is a parameter introduced here mainly to make $\lambda$ a dimensionless number and it can actually be taken as any real positive number. In practice, a preferable choice would be the integral length scale $l$ defined in eq. (2.5). Once the value of $L$ is determined, a constraint regarding $p(\lambda)$, or more specifically the expectation of $\lambda$, should be enforced such that the integral length scales of the synthetic velocity can coincide with those of eq. (2.5) exactly. We will discuss this issue later.

The initial position of an eddy with the scale of $\sigma$ is also an independent random variable, satisfying a uniform distribution in a bounding box $B(\sigma)$ surrounding $S$ defined as

$$B(\sigma) = \left\{\boldsymbol{x} = (x_1, x_2, x_3) \in \mathbb{R}^3 : x_{i,\min}(\sigma) < x_i < x_{i,\max}(\sigma)\right\}, \quad i \in \{1, 2, 3\}, \tag{2.8}$$

where $x_{i,\min}(\sigma)$ and $x_{i,\max}(\sigma)$ are the $\sigma$-dependent lower and upper bounds of box $B$ in the $x_i$-direction, respectively. We also use the use the function $V(\sigma)$ to the denote the volume of the box $B(\sigma)$. After initialization, eddies will be convected downstream with the mean velocity of $\boldsymbol{U}(\boldsymbol{x})$ and regenerated upstream once convected outside their bounding boxes.

With the above notation introduced, the turbulent velocity field synthesized by the proposed method writes

$$\boldsymbol{U}(\boldsymbol{x}, t) = \langle \boldsymbol{U}(\boldsymbol{x}) \rangle + \nabla \times \boldsymbol{\psi}(\boldsymbol{x}, t), \tag{2.9}$$

where the baskets denote the statistical mean and $\boldsymbol{\psi} = (\psi_1, \psi_2, \psi_3)$ is a synthetic vector potential field computed from

$$\boldsymbol{\psi}(\boldsymbol{x}, t) = \sqrt{\frac{\gamma}{N}} \sum_{m=1}^{N} \sqrt{\frac{V(\sigma^m)}{\sigma^m}} \boldsymbol{\epsilon}^m f\left(\frac{\|\boldsymbol{x} - \boldsymbol{x}^m(t)\|}{\sigma^m}\right). \tag{2.10}$$

In eq. (2.10) and the following context, $t$ denotes the time, $\gamma$ is a parameter characterizing the intensity of eddies, $\|\cdot\|$ represents the second-order norm, $\boldsymbol{x}^m$ and $\sigma^m$ are the location and length scale of the $m$-th eddy, respectively, and $\boldsymbol{\epsilon}^m = (\epsilon_1^m, \epsilon_2^m, \epsilon_3^m)$ is a vector of random signs in which $\epsilon_i^m \in \{1, -1\}$ has equal probability to take 1 or $-1$. The notation $f$ stands for a shape function describing the local distribution of the $\boldsymbol{\psi}$ field carried by each synthetic eddy. It is a continuous and first-order differentiable scalar function, denoted by $f(r) : \mathbb{R}^+ \to \mathbb{R}$ in this study, assumed to satisfy the following three assumptions:

i. The integral of $\int_0^\infty r^2 f^2(r)\,\mathrm{d}r$ exists and is bounded.
ii. The integral of $\int_0^\infty (r f'(r))^2\,\mathrm{d}r$, where $f'(r)$ stands for the derivative of $f(r)$, exists and is bounded.
iii. The derivative of $f(r)$ at $r = 0$ equals to zero, i.e., $f'(0) = 0$, which ensures the continuity of the velocity field induced by each synthetic eddy in space.

We further introduce the notation $\xi$ to denote a positive real constant such that the integral of $r^2 f^2(r)$ and $(r f'(r))^2$ on the interval of $[0, r_{\max}]$ with $r_{\max} \geq \xi$ can be considered to satisfy the approximations of

$$\int_0^{r_{\max}} r^2 f^2(r)\,\mathrm{d}r \approx \int_0^\infty r^2 f^2(r)\,\mathrm{d}r, \quad \int_0^{r_{\max}} (r f'(r))^2\,\mathrm{d}r \approx \int_0^\infty (r f'(r))^2\,\mathrm{d}r. \tag{2.11}$$

With the definition of $\xi$ introduced, the bounds of the box $B(\sigma)$ in the proposed method are determined by

$$x_{i,\min}(\sigma) = \min_{\boldsymbol{x} \in S}(x_i) - \xi\sigma, \quad x_{i,\max}(\sigma) = \max_{\boldsymbol{x} \in S}(x_i) + \xi\sigma. \tag{2.12}$$

The effect of determining the bounds of $B(\sigma)$ in terms of eq. (2.12) is to treat the shape function $f(r)$ as a truncated one, having a compact support on $[-\xi, \xi]$, when computing the synthetic velocity through eq. (2.9). The shape-function-dependent constant $\xi$ is required to be sufficiently large (with which the approximations of eq. (2.11) hold) in order that we can still regard $f(r)$ as the original (untruncated) function when analyzing the statistics of the synthetic velocity.

Finally, since the length scales of the eddies can be taken as any value within the interval of $[\lambda_{\min} L, \lambda_{\max} L]$, we name the proposed method as the continuous multi-scale synthetic eddy method (CMSSEM). Also note that the synthetic turbulence obtained from the proposed SEM obeys Taylor's frozen turbulence hypothesis [14], identical to other SEMs currently available in literature.

### *2.3. First and second-order statistics of the synthetic velocity*

Let $\boldsymbol{u}$ denote the fluctuating component of the synthetic velocity $\boldsymbol{U}$. The first and second-order statistics of the turbulent velocity $\boldsymbol{u}$ can be determined from those properties of the potential field $\boldsymbol{\psi}$ and its spatial derivatives. First, according to eq. (2.10), the mean value of the partial derivative of the $i$-th component of $\boldsymbol{\psi}$ with respect to $x_j$, i.e., $\partial\psi_i/\partial x_j$, writes

$$\left\langle \frac{\partial \psi_i}{\partial x_j}(\boldsymbol{x}) \right\rangle = \sqrt{\frac{\gamma}{N}} \sum_{m=1}^{N} \sqrt{\frac{V(\sigma^m)}{(\sigma^m)^3}} \left\langle \frac{\epsilon_i^m x_i}{\|\boldsymbol{x} - \boldsymbol{x}^m\|} f'\left(\frac{\|\boldsymbol{x} - \boldsymbol{x}^m\|}{\sigma^m}\right) \right\rangle. \tag{2.13}$$

where $\langle\cdot\rangle$ stand for the spatial average over box the bounding box $B$. The independence between the random variables $\epsilon_i^m$ and $\boldsymbol{x}^m$ indicates that

$$\left\langle \frac{\epsilon_i^m x_i}{\|\boldsymbol{x} - \boldsymbol{x}^m\|} f'\left(\frac{\|\boldsymbol{x} - \boldsymbol{x}^m\|}{\sigma^m}\right) \right\rangle = \langle \epsilon_i^m \rangle \left\langle \frac{x_i}{\|\boldsymbol{x} - \boldsymbol{x}^m\|} f'\left(\frac{\|\boldsymbol{x} - \boldsymbol{x}^m\|}{\sigma^m}\right) \right\rangle. \tag{2.14}$$

Since $\langle \epsilon_i^m \rangle = 0$, we obtain $\langle \partial\psi_i(\boldsymbol{x})/\partial x_j \rangle = 0$ and consequently $\langle \boldsymbol{u} \rangle = \boldsymbol{0}$.

By definition, the two-point correlation tensor of the vector field $\boldsymbol{\psi}$ writes

$$R_{ij}^{\psi}(\boldsymbol{x},\boldsymbol{r}) = \langle \psi_i(\boldsymbol{x})\psi_j(\boldsymbol{x}+\boldsymbol{r})\rangle, \tag{2.15}$$

where $\boldsymbol{r}$ is a vector defining the relative positions between the two points at which the vector $\boldsymbol{\psi}$ is computed. From eq. (2.10) and the linearity of the statistical mean, we have

$$R_{ij}^{\psi}(\boldsymbol{x},\boldsymbol{r}) = \frac{\gamma}{N}\sum_{m=1}^{N}\sum_{n=1}^{N}\sqrt{\frac{V(\sigma^m)V(\sigma^n)}{\sigma^m\sigma^n}}\left\langle \epsilon_i^m\epsilon_j^n f\left(\frac{\|\boldsymbol{x}-\boldsymbol{x}^m\|}{\sigma^m}\right) f\left(\frac{\|\boldsymbol{x}+\boldsymbol{r}-\boldsymbol{x}^n\|}{\sigma^n}\right)\right\rangle. \tag{2.16}$$

Using again the independence between the positions $\boldsymbol{x}^m$ and random signs $\boldsymbol{\epsilon}^m$ of the eddies, we obtain

$$R_{ij}^{\psi}(\boldsymbol{x},\boldsymbol{r}) = \begin{cases} \dfrac{\gamma}{N}\displaystyle\sum_{m=1}^{N}\frac{V(\sigma^m)}{\sigma^m}\left\langle f\left(\frac{\|\boldsymbol{x}-\boldsymbol{x}^m\|}{\sigma^m}\right) f\left(\frac{\|\boldsymbol{x}+\boldsymbol{r}-\boldsymbol{x}^m\|}{\sigma^m}\right)\right\rangle & i=j, \\ 0 & i\neq j. \end{cases} \tag{2.17}$$

Since $\boldsymbol{x}^m$ is uniformly distributed in $B(\sigma^m)$, the spatially-averaged term in eq. (2.17) can be evaluated from the integral

$$\frac{1}{V(\sigma^m)}\int_{B(\sigma^m)} f\left(\frac{\|\boldsymbol{x}-\boldsymbol{y}\|}{\sigma^m}\right) f\left(\frac{\|\boldsymbol{x}+\boldsymbol{r}-\boldsymbol{y}\|}{\sigma^m}\right)\mathrm{d}\boldsymbol{y}. \tag{2.18}$$

Using the first approximation of eq. (2.11), the integral in eq. (2.18) can be rewritten as

$$\int_{\mathbb{R}^3} f\left(\frac{\|\boldsymbol{x}\|}{\sigma^m}\right) f\left(\frac{\|\boldsymbol{r}-\boldsymbol{x}\|}{\sigma^m}\right)\mathrm{d}\boldsymbol{x}. \tag{2.19}$$

When $N$ is sufficiently large, we have from eq. (2.6) that

$$\frac{1}{N}\sum_{m=1}^{N}\frac{1}{\sigma^m}\int_{\mathbb{R}^3} f\left(\frac{\|\boldsymbol{x}\|}{\sigma^m}\right) f\left(\frac{\|\boldsymbol{r}-\boldsymbol{x}\|}{\sigma^m}\right)\mathrm{d}\boldsymbol{x} = L^2\int_{\lambda_{\min}}^{\lambda_{\max}}\lambda^2[f*f]\left(\frac{\boldsymbol{r}}{\lambda L}\right)p(\lambda)\,\mathrm{d}\lambda, \tag{2.20}$$

where

$$[f*f](\boldsymbol{r}) = \int_{\mathbb{R}^3} f(\|\boldsymbol{x}\|)f(\|\boldsymbol{r}-\boldsymbol{x}\|)\,\mathrm{d}\boldsymbol{x}. \tag{2.21}$$

Inserting eq. (2.20) into eq. (2.17), this yields

$$R_{ij}^{\psi}(\boldsymbol{x},\boldsymbol{r}) = \begin{cases} \gamma L^2\displaystyle\int_{\lambda_{\min}}^{\lambda_{\max}}\lambda^2[f*f]\left(\frac{\boldsymbol{r}}{\lambda L}\right)p(\lambda)\,\mathrm{d}\lambda & i=j, \\ 0 & i\neq j. \end{cases} \tag{2.22}$$

The spectrum tensor of the synthetic vector field $\psi$, denoted as $\Phi_{ij}^{\psi}(\boldsymbol{\kappa})$, can then be obtained through the three-dimensional Fourier transform of the correlation tensor, i.e.,

$$\Phi_{ij}^{\psi}(\boldsymbol{\kappa}) = \begin{cases} \dfrac{1}{8\pi^3}F_{\boldsymbol{\kappa}}\{R_{ij}^{\psi}(\boldsymbol{r})\} & i=j, \\ 0 & i\neq j, \end{cases} \tag{2.23}$$

in which $F_{\boldsymbol{\kappa}}$ stands for the Fourier transform operator. For a general vector variable function $g(\boldsymbol{x}):\mathbb{R}^3\to\mathbb{R}$, $F_{\boldsymbol{\kappa}}$ can be expressed as

$$F_{\boldsymbol{\kappa}}\{g(\boldsymbol{x})\} = \iiint_{-\infty}^{\infty} g(\boldsymbol{x})e^{-i\boldsymbol{\kappa}\cdot\boldsymbol{x}}\,\mathrm{d}\boldsymbol{x}. \tag{2.24}$$

To derive a more straightforward relation regarding the spectrum tensor of $\psi$, we examine the Fourier transform of the vector variable function $f(\|\boldsymbol{x}\|)$ in eq. (2.21). Considering the spherical symmetry of $f(\|\boldsymbol{x}\|)$, its Fourier transform should also be a spherically symmetric function (denoted by $F(\kappa)$ hereafter) and satisfy

$$F_{\boldsymbol{\kappa}}\left\{f(\|\boldsymbol{x}\|)\right\} = F(\kappa) = 4\pi \int_0^\infty \frac{\sin \kappa r}{\kappa r} r^2 f(r)\,\mathrm{d}r. \tag{2.25}$$

where $\kappa = \|\boldsymbol{\kappa}\|$. With the use of the convolution theorem, we have

$$F_{\boldsymbol{\kappa}}\left\{[f * f]\left(\frac{\boldsymbol{r}}{\lambda L}\right)\right\} = \lambda^3 L^3 F^2(\lambda L \kappa). \tag{2.26}$$

Using the above relation, the spectrum tensor $\Phi_{ij}^{\psi}(\boldsymbol{\kappa})$ can be rewritten as

$$\Phi_{ij}^{\psi}(\boldsymbol{\kappa}) = \begin{cases} \dfrac{\gamma L^5}{8\pi^3} \displaystyle\int_{\lambda_{\min}}^{\lambda_{\max}} \lambda^5 F^2(\lambda L \kappa) p(\lambda)\,\mathrm{d}\lambda & i = j, \\ 0 & i \neq j. \end{cases} \tag{2.27}$$

Based on the equality of $\boldsymbol{u} = \nabla \times \boldsymbol{\psi}$, we have the energy spectrum tensor of the synthetic velocity in the form of

$$\Phi_{ij}(\boldsymbol{\kappa}) = \begin{bmatrix} \kappa_2^2 \Phi_{33}^{\psi} + \kappa_3^2 \Phi_{22}^{\psi} & -\kappa_1 \kappa_2 \Phi_{33}^{\psi} & -\kappa_1 \kappa_3 \Phi_{22}^{\psi} \\ -\kappa_1 \kappa_2 \Phi_{33}^{\psi} & \kappa_1^2 \Phi_{33}^{\psi} + \kappa_3^2 \Phi_{11}^{\psi} & -\kappa_2 \kappa_3 \Phi_{11}^{\psi} \\ -\kappa_1 \kappa_3 \Phi_{22}^{\psi} & -\kappa_2 \kappa_3 \Phi_{11}^{\psi} & \kappa_1^2 \Phi_{22}^{\psi} + \kappa_2^2 \Phi_{11}^{\psi} \end{bmatrix}. \tag{2.28}$$

Introducing the notation

$$\Phi^{\psi}(\kappa) = \frac{\gamma L^5}{8\pi^3} \int_{\lambda_{\min}}^{\lambda_{\max}} \lambda^5 F^2(\lambda L \kappa) p(\lambda)\,\mathrm{d}\lambda, \tag{2.29}$$

the energy spectrum tensor of the synthetic velocity can be simplified as

$$\Phi_{ij}(\boldsymbol{\kappa}) = \Phi^{\psi}(\kappa)\left(\kappa^2 \delta_{ij} - \kappa_i \kappa_j\right). \tag{2.30}$$

Thus, for the generation of HIT with an energy spectrum tensor of eq. (2.1), it is only required to select a particular shape function $f(r)$ and a probability distribution $p(\lambda)$, with which the equality

$$\frac{\gamma L^5}{8\pi^3} \int_{\lambda_{\min}}^{\lambda_{\max}} \lambda^5 F^2(\lambda L \kappa) p(\lambda)\,\mathrm{d}\lambda = \frac{E(\kappa)}{4\pi \kappa^4}, \tag{2.31}$$

holds exactly in the CMSSEM. Before the discussion on this issue, we would like to further investigate the Reynolds stresses and integral length scales of the synthetic velocity. Integrating the sum of the diagonal components of the energy spectrum tensor $\Phi_{ij}(\boldsymbol{\kappa})$ given by eq. (2.28) over all $\boldsymbol{\kappa}$-space, this yields

$$\iiint_{-\infty}^{\infty} \Phi_{ii}(\boldsymbol{\kappa})\,\mathrm{d}\boldsymbol{\kappa} = \frac{\gamma L^5}{4\pi^3} \int_0^\infty 4\pi \kappa^2 \left(\kappa^2 \int_{\lambda_{\min}}^{\lambda_{\max}} \lambda^5 F^2(\lambda L \kappa)\,\mathrm{d}\lambda\right)\mathrm{d}\kappa \tag{2.32}$$

Changing the sequence of the double integrals on the right hand side of eq. (2.32) and using the normalization eq. (2.7), we obtain

$$\frac{\gamma L^5}{4\pi^3} \int_0^\infty 4\pi \kappa^2 \left(\kappa^2 \int_{\lambda_{\min}}^{\lambda_{\max}} \lambda^5 F^2(\lambda L \kappa)\,\mathrm{d}\lambda\right)\mathrm{d}\kappa = \frac{\gamma}{\pi^2} \int_0^\infty \kappa^4 F^2(\kappa)\,\mathrm{d}\kappa. \tag{2.33}$$

One can also easily verify that the integral of any off-diagonal component in eq. (2.28) over all $\boldsymbol{\kappa}$-space equals to zero. Thus, the Reynolds stress tensor of the synthetic velocity can be written as

$$\tau_{ij} = \begin{cases} \frac{\gamma}{3\pi^2} \int_0^\infty \kappa^4 F^2(\kappa)\,\mathrm{d}\kappa & i = j, \\ 0 & i \neq j. \end{cases} \tag{2.34}$$

Comparing eq. (2.34) to eq. (2.3), we have an equality regarding the Fourier transform of $f(r)$ that has the form

$$\frac{\tau}{\gamma} = \frac{1}{3\pi^2}\int_0^\infty \kappa^4 F^2(\kappa)\,\mathrm{d}\kappa. \tag{2.35}$$

It can be shown that the above equality is equivalent to

$$\frac{\tau}{\gamma} = \frac{8\pi}{3}\int_0^\infty (r f'(r))^2\,\mathrm{d}r. \tag{2.36}$$

Apparently, eq. (2.35) or eq. (2.36) should be satisfied by the employed the shape function $f(r)$ and the eddy intensity parameter $\gamma$ in order that the Reynolds stress tensor of the synthetic velocity can match with that of eq. (2.2) exactly. This also explains the necessity of the second assumption concerning $f(r)$.

Next, we consider the energy spectrum of the $x_1$-component velocity which writes

$$\Phi_{11}(\boldsymbol{\kappa}) = \frac{\gamma L^5}{8\pi^3}(\kappa_2^2+\kappa_3^2)\int_{\lambda_{\min}}^{\lambda_{\max}} \lambda^5 F^2(\lambda L\kappa) p(\lambda)\,\mathrm{d}\lambda. \tag{2.37}$$

The integral length scale of the $x_1$-component velocity in the $x_1$-direction can be computed from

$$L_{11}^{(1)} = \frac{\pi}{\tau}\iint_{-\infty}^{\infty} \Phi_{11}(0,\kappa_2,\kappa_3)\,\mathrm{d}\kappa_2\,\mathrm{d}\kappa_3. \tag{2.38}$$

Inserting eqs. (2.35) and (2.37) into eq. (2.38), we arrive at

$$L_{11}^{(1)} = \frac{3\pi\langle\lambda\rangle L}{4}\frac{\int_0^\infty \kappa^3 F^2(\kappa)\,\mathrm{d}\kappa}{\int_0^\infty \kappa^4 F^2(\kappa)\,\mathrm{d}\kappa}, \tag{2.39}$$

where $\langle\lambda\rangle$ stands for the expectation of $\lambda$, i.e.,

$$\langle\lambda\rangle = \int_{\lambda_{\min}}^{\lambda_{\max}} \lambda p(\lambda)\,\mathrm{d}\lambda. \tag{2.40}$$

Following the same procedure, the other integral length scales of the synthetic velocity can be shown to satisfy

$$L_{ii}^{(j)} = \begin{cases} \frac{3}{4}\pi\langle\lambda\rangle L\int_0^\infty \kappa^3 F^2(\kappa)\,\mathrm{d}\kappa\cdot\left(\int_0^\infty \kappa^4 F^2(\kappa)\,\mathrm{d}\kappa\right)^{-1} & i=j, \\ \frac{3}{8}\pi\langle\lambda\rangle L\int_0^\infty \kappa^3 F^2(\kappa)\,\mathrm{d}\kappa\cdot\left(\int_0^\infty \kappa^4 F^2(\kappa)\,\mathrm{d}\kappa\right)^{-1} & i\neq j. \end{cases} \tag{2.41}$$

Comparing eq. (2.41) to eq. (2.5), we find that the integral length scales of the synthetic velocity can coincide with those of eq. (2.5) exactly on the condition of

$$\frac{\langle\lambda\rangle L}{l} = \frac{4\int_0^\infty \kappa^4 F^2(\kappa)\,\mathrm{d}\kappa}{3\pi\int_0^\infty \kappa^3 F^2(\kappa)\,\mathrm{d}\kappa}. \tag{2.42}$$

When $f(r)$ and $p(\lambda)$ are both available, the parameters of $\gamma$ and $L$ can be computed from eqs. (2.35) and (2.42) directly. On the contrary, with prescribed values of $\gamma$ and $L$, $f(r)$ and $p(\lambda)$ should enforce the equality of eq. (2.31).

### *2.4. Determination of the eddy-scale probability distribution*

Although it is theoretically possible to obtain either $f(r)$ or $p(\lambda)$ from eq. (2.31) when one of the two functions is given apriori, it is suggested to let $f(r)$ be the known term and solve eq. (2.31) for $p(\lambda)$ in most cases. This is because integral functions like eq. (2.31) can only be solved numerically in general. Considering the derivative of $f(r)$ will be repeatedly evaluated during the synthesis of turbulence, it is good to have $f'(r)$ as a function which can be directly and efficiently evaluated. If only the numerical solution of $f(r)$ is available, it would take considerable effort to compute its derivatives for different $r$, let alone the existence of the numerical error in approximating $f'(r)$ from the discrete values of $f(r)$.

Once $f(r)$ is given in prior, the term $F^2(\lambda L\kappa)$ in eq. (2.31), as well as the eddy intensity parameter $\gamma$, will then be explicitly known. Meanwhile, a preferred value can be chosen for the parameter of $L$. Now, we rewrite eq. (2.31) by replacing the variable $\kappa$ in the equality with $\kappa/L$, this yields

$$\int_{\lambda_{\min}}^{\lambda_{\max}} \lambda^5 F^2(\lambda\kappa)\, p(\lambda)\, \mathrm{d}\lambda = 2\pi^2 \frac{E(\kappa/L)}{\gamma L \kappa^4}. \tag{2.43}$$

The above equation defines a Fredholm integral equation of the first kind [15], in which the term $\lambda^5 F^2(\lambda\kappa)$ can be considered as the kernel and $p(\lambda)$ as the unknown function to be solved for. In general, eq. (2.43) should be solved numerically for an arbitrary energy spectrum function $E(\kappa)$. In some special cases, however, there may exist an analytic solution to eq. (2.43) for a particular $E(\kappa)$. Apart from solving eq. (2.43) directly, we can also approximate its solution by expressing $p(\lambda)$ as a particular function with some unknown parameters. The parameters are then optimized through minimizing the difference between the energy spectrum $E(\kappa)$ computed from eq. (2.31) and the target one. During the optimization, eq. (2.42) can be used as a constraint regarding $p(\lambda)$.

It is noted that the CMSSEM reduces to a single-scale divergence-free synthetic eddy method, basically equivalent to the method of [4], if $p(\lambda)$ admits the form of

$$p(\lambda) = \delta(\lambda - 1), \tag{2.44}$$

where $\delta$ denotes the Dirac delta function. When eq. (2.44) holds, eq. (2.43) can be further simplified as

$$F^2(\kappa) = 2\pi^2 \frac{E(\kappa/L)}{\gamma L \kappa^4}. \tag{2.45}$$

One can easily verify that the $F^2(\kappa)$ given by eq. (2.45) satisfy eqs. (2.35) and (2.42) exactly on the condition of eq. (2.44). Based on eq. (2.45), the shape function $f(r)$ can be determined by

$$f(r) = \frac{1}{2\pi^2}\int_0^\infty \frac{\sin(\kappa r)}{\kappa r}\kappa^2\sqrt{F^2(\kappa)}\,\mathrm{d}\kappa = \frac{L}{2\pi}\sqrt{\frac{2}{L}}\int_0^\infty \frac{\sin(\kappa r)}{\kappa r}\sqrt{\frac{E(\kappa/L)}{\gamma}}\,\mathrm{d}\kappa, \tag{2.46}$$

for prescribed $\gamma$, $L$ and $E(\kappa)$.

## 3. Numerical issues related to the application of the CMSSEM

This section mainly discuss some numerical issues concerning the application of the CMSSEM in practice.

### *3.1. Some choices for the shape function*

As mentioned earlier, the shape function in the CMSSEM is suggested to be explicitly specified apriori. Here, we present four examples of $f(r)$, including a Gauss function, a Mexican-hat function, a Bessel function and an exponential function, their derivatives and corresponding $F(\kappa)$ in Table 1 and fig. 1 for reference. The constant coefficients in the presented shape functions are specially tuned so that the right hand sides of eqs. (2.35) and (2.42) corresponding to them all equal to 1. As a result, the $\gamma$, $L$ and $p(\lambda)$ employed together with each of these shape functions should satisfy $\gamma = \tau$ and $\langle\lambda\rangle L = l$ so that the conditions of eqs. (2.35) and (2.42) can be meet.

For the special case of $p(\lambda) = \delta(\lambda - 1)$, the energy spectrum functions of the synthetic turbulence generated by the CMSSEM with the presented shape functions respectively, are also listed in Table 1. fig. 1c demonstrates the shape of those spectra within a dimensionless wavenumber range of $l\kappa \in [10^{-1}, 10^2]$. The Gauss and the Mexican-hat functions, with a flatter slope at the eddy-center region, result in energy spectrum functions decaying exponentially for larger $\kappa$. In comparison, the Bessel and the exponential functions, characterized by a sharper peak at the eddy-center region, produce energy spectrum functions decaying as $\kappa^{-6}$ and $\kappa^{-8}$ respectively for larger $\kappa$. This indicates that the slope of the shape function at the eddy-center region affects the decay of $E(\kappa)$ in the energy dissipation range of the synthetic turbulence greatly.

A factor that may affect our selection of the shape function is the constant parameter $\xi$ depending on it, as this parameter affects the volumes of eddies' bounding boxes directly. To compare the values of $\xi$ corresponding to different shape functions, we introduce the notation

$$\Omega(\xi) = \max\left\{1 - \frac{\int_0^\xi r^2 f^2(r)\,\mathrm{d}r}{\int_0^\infty r^2 f^2(r)\,\mathrm{d}r},\ 1 - \frac{\int_0^\xi (r f'(r))^2\,\mathrm{d}r}{\int_0^\infty (r f'(r))^2\,\mathrm{d}r}\right\}, \tag{3.1}$$

which equals to zero as $\xi \to \infty$. Table 2 gives the values of $\xi$ with which $\Omega$ equals to $10^{-6}$ for the presented shape functions.

Apart from $\xi$, another shape-function-related parameter has also to be specified, that is, the number of eddies $N$. From statistical point of view, it should be sufficiently large such that, for each point in the point set $S$, there exists at least one eddy having considerable contribution to the synthetic velocity on this point. In the original SEM of [1] where eddies are of a universal length scale $\sigma$, $N$ is obtained by dividing the volume of eddies' bounding box with the third power of $2\sigma$ (for the three dimensional case). By doing so, the averaged distance of the synthetic eddies in the $x_i$-directions ($i \in \{1,2,3\}$) should equal to $2\sigma$. Also note that the shape function in [1] is assumed to have a compact support on $[-1,1]$. In comparison, the scales of the eddies vary from $\lambda_{\min}L$ to $\lambda_{\max}L$ in the CMSSEM and the shape function is considered to have a compact support on $[-\xi,\xi]$ (when computing the synthetic velocity). Considering these differences, it is suggested to determine the $N$ in the CMSSEM in terms of

$$N \approx \frac{V(\lambda_{\min}L)}{(2\xi\lambda_{\min}L)^3}. \tag{3.2}$$

We use the approximation symbol in the above relation to express the opinion that it is not essentially required to determine $N$ from eq. (3.2) exactly. The determination of $N$ is a case-independent issue and should also take the related computational effort into account. Also note that, unless the point set $S$ only has a single point, the term on the right hand side of eq. (3.2) is a monotonically decreasing function of $\lambda_{\min}$. To avoid the overestimation of $N$ due to the use of a extremely small $\lambda_{\min}$, we suggest to set a lower bound for $\lambda_{\min}$ according to

$$\lambda_{\min} \geq \frac{\min(\Delta_i, \Delta t)}{\xi}, \tag{3.3}$$

where $\Delta_i$ denotes the (smallest) distance of the points in $S$ along the $x_i$-direction and $\Delta t$ stands for the time-step size. The use of eq. (3.3) is based on fact that eddies with scales smaller than $\Delta_i/\xi$ and $\Delta t/\xi$ do not result in spatially or temporally correlated velocity fields on the point set $S$. In other words, the synthetic velocity induced by those eddies are just white noises. It is therefore reasonable to exclude them from the synthetic eddy set in the CMSSEM.

Table 1: Examples of the shape function $f(r)$: the notation $\alpha$ stands for a constant which equals to $24\sqrt{\pi}/35$, $8/3$ and $16/5$ in the Mexican-hat, Bessel and exponential functions, respectively; $K$ denotes the modified Bessel function of the second kind.

| Type | $f(r)$ | $f'(r)$ | $F(\kappa)$ | $E(\kappa)$ for $p(\lambda) = \delta(\lambda - 1)$ |
|---|---|---|---|---|
| Gauss | $\frac{1}{\sqrt{\pi}} e^{-\frac{\pi r^2}{2}}$ | $-\sqrt{\pi} r e^{-\frac{\pi r^2}{2}}$ | $\sqrt{\frac{8}{\pi}} e^{-\frac{\kappa^2}{2\pi}}$ | $\frac{4\tau l^5 \kappa^4}{\pi^3} e^{-\frac{l^2\kappa^2}{\pi}}$ |
| Mexican-hat | $\frac{6\alpha^{1/2}}{\sqrt{35}\pi^{3/4}} \left(1 - \frac{\alpha^2 r^2}{3}\right) e^{-\frac{\alpha^2 r^2}{2}}$ | $\frac{2\alpha^{5/2} r(\alpha^2 r^2 - 5)}{\sqrt{35}\pi^{3/4}} e^{-\frac{\alpha^2 r^2}{2}}$ | $\sqrt{\frac{32}{35}} \frac{\pi^{3/4}\kappa^2}{\alpha^{9/2}} e^{-\frac{\kappa^2}{2\alpha^2}}$ | $\frac{16\tau l^9 \kappa^8}{35\alpha^9\sqrt{\pi}} e^{-\frac{l^2\kappa^2}{\alpha^2}}$ |
| Bessel | $\frac{\alpha^{5/2} r K_1(\alpha r)}{\pi^{3/2}}$ | $\frac{\alpha^{5/2} K_1(\alpha r)}{\pi^{3/2}} - \frac{\alpha^{7/2} r[K_0(\alpha r) + K_2(\alpha r)]}{2\pi^{3/2}}$ | $\frac{6\alpha^{7/2}\pi^{1/2}}{(\alpha^2+\kappa^2)^{5/2}}$ | $\frac{128\alpha^5 \tau l^5 \kappa^4}{\pi(\alpha^2 + l^2\kappa^2)^5}$ |
| Exponential | $\sqrt{\frac{24}{15\pi}} (1 + \alpha r) e^{-\alpha r}$ | $-\sqrt{\frac{8}{5\pi}} \alpha^2 r e^{-\alpha r}$ | $\sqrt{\frac{2\pi}{5}} \frac{64\alpha^3}{(\alpha^2+\kappa^2)^3}$ | $\frac{4096\alpha^5 \tau l^5 \kappa^4}{5\pi(\alpha^2 + l^2\kappa^2)^6}$ |

Table 2: Suggested values for the parameter $\xi$ corresponding to the shape functions listed in Table 1.

| Type | Gauss | Mexican-hat | Bessel | Exponential |
|---|---|---|---|---|
| $\xi$ for $\Omega = 10^{-6}$ | 2.3899 | 3.8439 | 4.0252 | 3.7464 |

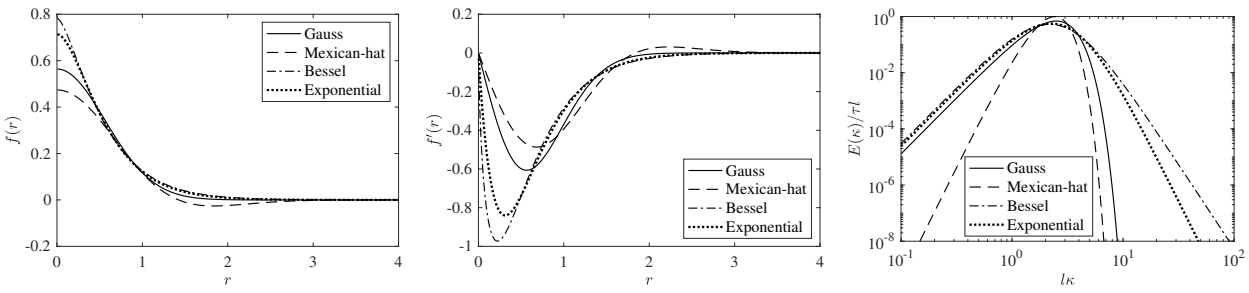


(a) $f(r)$ (b) $f'(r)$ (c) $E(\kappa)$ for $p(\lambda) = \delta(\lambda - 1)$

Figure 1: The shape functions listed in Table 1, their derivatives and resulting energy spectrum functions for the HIT generated by the CMSSEM with $p(\lambda) = \delta(\lambda - 1)$.

### *3.2. Initialization and regeneration of synthetic eddies*

In light of the work of [1], the initialization and regeneration of the eddies in the CMSSEM can be carried out in the following steps:

(a) Generate for eddy $m \in \{1, ..., N\}$ a random scalar $\lambda^m \in [\lambda_{\min}, \lambda_{\max}]$ according to the PDF of $p(\lambda)$ and compute its scale in terms of $\sigma^m = \lambda^m L$.
(b) Define for eddy $m$ a box $B(\sigma^m)$ according to eq. (2.8) and calculate the volume of the box $B(\sigma^m)$.
(c) Generate for eddy $m$ two random vectors $\boldsymbol{x}^m \in B(\sigma^m)$ and $\boldsymbol{\epsilon}^m$ for its location and random sign, respectively.
(d) Compute the synthetic velocity field $\boldsymbol{U}$ from eq. (2.9) at the current time-instant $t$.
(e) Update the locations of the eddies in terms of $\boldsymbol{x}^m(t + \Delta t) = \boldsymbol{x}^m(t) + \langle \boldsymbol{U} \rangle \Delta t$ and identify the eddies (denoted by the index set $I$) which are convected outside of their bounding boxes, i.e., $\boldsymbol{x}^m(t + \Delta t) \notin B(\sigma^m)$ for $m \in I$.
(f) Regenerate for eddy $m \in I$ a random scalar $\lambda^m$ according to a different PDF (denoted by $\tilde{p}(\lambda)$ in the following context) and update its bounding box according to its current scale $\sigma^m = \lambda^m L$.
(g) Regenerate for eddy $m \in I$ two random vectors $\boldsymbol{x}^m \in B_{\Delta t}(\sigma^m)$ and $\boldsymbol{\epsilon}^m$ for its new location and random sign, respectively.
(h) Compute the synthetic velocity field $\boldsymbol{U}$ at $t + \Delta t$ by returning to step (d).

There are two worth-mentioning features in the above stated procedures that differ from conventional approach due to the multi-scale characteristic of the synthetic eddies in the CMSSEM. First, the region $B_{\Delta t}(\sigma)$ considered in step (g) is defined as

$$B_{\Delta t}(\sigma) = \{\boldsymbol{x} \in B(\sigma),\ (\boldsymbol{x} - \Delta t \boldsymbol{U}) \notin B(\sigma)\}. \tag{3.4}$$

Second, the newly generated $\lambda$ in step (f) should satisfy a probability distribution different from the original $p(\lambda)$ in step (a). To explain this, we consider a time instant after which all eddies initially generated in step (c) have been convected outside of their bounding boxes. That is to say, all remaining eddies are the ones generated in step (g) and they need to travel across the entire span of their bounding boxes before the regeneration. Note that the span of the bounding boxes depends on $\lambda$ based on eq. (2.8). Since all eddies move with the same velocity, the time it takes for an eddy to be convected outside its bounding box is $\lambda$-dependent. Thus, the $\lambda$ of the eddies, which have been convected outside their bounding boxes, no longer satisfy $p(\lambda)$ and we denote their current probability distribution by $\tilde{p}(\lambda)$. Without loss of generality, we assume that the mean velocity $\langle \boldsymbol{U} \rangle$ is aligned with the $x_i$-direction. In this case, the $\tilde{p}(\lambda)$ can be proven to satisfy

$$\tilde{p}(\lambda) \propto \frac{p(\lambda)}{\underset{x_i}{\text{span}}\,(B(\lambda L))}, \tag{3.5}$$

where the denominator in eq. (3.5) refers to its span in the $x_i$-direction. Apparently, the PDF used for the determination of the new $\lambda$ (assigned to the regenerated eddies) should equal to $\tilde{p}(\lambda)$ in order that the $\lambda$ of all present eddies can still satisfy the PDF of $p(\lambda)$.

From the generation process introduced above, it is easy to see that each eddy will be assigned to a new random $\lambda$ at both the eddy initialization and regeneration stages. As the synthetic process continuously proceeds with the time-step increasing, the probability distribution of all $\lambda$ that have been assigned to present and previous eddies will finally converge to $p(\lambda)$. Consequently, the energy spectrum of the synthetic turbulence can also converge to the desired one exactly according to eq. (2.43).

### *3.3. Generation of periodic synthetic fields*

In many numerical experiments, the synthetic turbulence is required to be periodic in certain directions to cater for the periodicity of computational domains in those directions. For the CMSSEM, the periodicity of the synthetic potential field $\boldsymbol{\psi}(\boldsymbol{x})$ and the velocity field $\boldsymbol{U}(\boldsymbol{x})$ can be achieved by making the eddies periodic in the required directions. Without loss of generality, we consider a case in which the velocity field is required to be periodic in all three directions with the periods of $\boldsymbol{P} = (P_1, P_2, P_3)$ satisfying

$$P_i = \max_{\boldsymbol{x}\in S}(x_i) - \min_{\boldsymbol{x}\in S}(x_i) \geq 2\xi\lambda_{\max}L. \tag{3.6}$$

Now that the eddies are periodic in space, the synthetic potential field $\boldsymbol{\psi}(\boldsymbol{x})$ in the CMSSEM should be computed with

$$\boldsymbol{\psi}(\boldsymbol{x}) = \sqrt{\frac{\gamma}{N}}\sum_{\boldsymbol{n}}\sum_{m}\sqrt{\frac{V_P}{\sigma^m}}\boldsymbol{\epsilon}^m f\left(\frac{\boldsymbol{x}-\boldsymbol{x}^m-\boldsymbol{n}\otimes\boldsymbol{P}}{\sigma^m}\right), \tag{3.7}$$

where $V_P = P_1P_2P_3$ and $\boldsymbol{n} = (n_1, n_2, n_3)$ with $n_i \in \mathbb{N}$. In eq. (3.7), the location of the $m$-th eddy, i.e., $\boldsymbol{x}^m$, follows a uniform distribution over a box $B_P$ defined as

$$B_P = \left\{\boldsymbol{x} = (x_1, x_2, x_3) \in \mathbb{R}^3 : \min_{\boldsymbol{x}\in S}(x_i) < x_i < \max_{\boldsymbol{x}\in S}(x_i)\right\}. \tag{3.8}$$

As the shape function $f(r)$ decays rapidly with the increase of $r$, it is reasonable to assume that the approximation

$$\sum_{\boldsymbol{n}} f\left(\frac{\boldsymbol{x}-\boldsymbol{x}^m-\boldsymbol{n}\otimes\boldsymbol{P}}{\sigma^m}\right) \approx f\left(\frac{\boldsymbol{x}-\tilde{\boldsymbol{x}}^m}{\sigma^m}\right), \tag{3.9}$$

holds under the assumption of eq. (3.6). The vector $\tilde{\boldsymbol{x}}^m = (\tilde{x}_1^m, \tilde{x}_2^m, \tilde{x}_3^m)$ in eq. (3.9) stands for a modified position computed as

$$\tilde{x}_i^m = x_i^m + nP_i, \tag{3.10}$$

where $n = \operatorname{argmin}\left(|x_i - x_i^m - nP_i|\right) \in \mathbb{N}$. Using eq. (3.9), eq. (3.7) can then be simplified as

$$\boldsymbol{\psi}(\boldsymbol{x}) = \sqrt{\frac{\gamma}{N}}\sum_{m=1}^{N}\sqrt{\frac{V_P}{\sigma^m}}\boldsymbol{\epsilon}^m f\left(\frac{\boldsymbol{x}-\tilde{\boldsymbol{x}}^m}{\sigma^m}\right). \tag{3.11}$$

Inserting eq. (3.11) into eq. (2.9) yields the desired periodic turbulent velocity field.

### *3.4. Imposing the divergence-free constraint on a finite volume grid*

The continuous velocity field generated by the CMSSEM or any other divergence-free synthetic eddy method is, with no doubt, divergence free. However, the turbulent velocities at discrete points do not satisfy the spatially discretized continuity equation in general because of the spatial discretization error. Failing to satisfy the continuity equation may result in strong disturbances in pressure during the solution of the Navier-Stokes equation, which will in turn alter the velocity field. The statistical properties of the corrected velocities usually differ from those of the original synthetic velocities and the differences between them depend largely on the residue of the continuity equation regarding the original synthetic velocity field.

To resolve this issue, a way will be to let the original synthetic velocity field satisfy the discretized continuity equation in the first place. Taking the finite volume grid as an example, this goal can be achieved by computing the velocity at a cell-face as the face-averaged synthetic velocity, i.e., the surface integral of the continuous synthetic

velocity field divided by the area of the cell face. For some special shape functions, there exists an analytic expression for the evaluation of the face-averaged synthetic velocity on cell-faces with regular shapes. In this case, the implementation of this approach does not result in too much additional computational effort. The earlier introduced Gauss-type shape function in Table 1 happens to meet this requirement. For a rectangular cell-face, normal to the $x_1$-direction, with a dimension of $\Delta_2 \times \Delta_3$, the $x_1$-component face-averaged synthetic velocity admits the form of

$$\begin{aligned} u_1(x) = \frac{1}{\Delta_2\Delta_3}\sqrt{\frac{\gamma}{N}}\sum_{m=1}^{N}\sqrt{\frac{V(\sigma^m)}{\sigma^m}}\Big\{\frac{\sigma^m}{\sqrt{2\pi}}\exp\Big[-\frac{\pi}{2}\Big(\frac{x_1-x_1^m}{\sigma^m}\Big)^2\Big] \\ \cdot\Big[\epsilon_3^m\bar{f}(x_2-x_2^m,\Delta_2,\sigma^m)\tilde{f}(x_3-x_3^m,\Delta_3,\sigma^m)-\epsilon_2^m\tilde{f}(x_2-x_2^m,\Delta_2,\sigma)\bar{f}(x_3-x_3^m,\Delta_3,\sigma^m)\Big]\Big\} \end{aligned} \tag{3.12}$$

where $\bar{f}$ and $\tilde{f}$ stand for functions of the form

$$\bar{f}(x,\Delta,\sigma) = \exp\Big(-\frac{\pi x^2}{2}\Big)\Big|_{(x-\Delta/2)/\sigma}^{(x+\Delta/2)/\sigma}, \quad \tilde{f}(x,\Delta,\sigma) = \mathrm{erf}\Big(\sqrt{\frac{\pi}{2}}x\Big)\Big|_{(x-\Delta/2)/\sigma}^{(x+\Delta/2)/\sigma}. \tag{3.13}$$

Similar relations can be derived for the other two velocity components $u_2$ and $u_3$, which are omitted here for simplicity. Finally, it should be mentioned that the face-averaging operation tends to flatten the local velocity fluctuations caused by small scale eddies. As a result, the energy spectrum function of the face-averaged synthetic velocity can be noticeably lower than that of the original synthetic velocity at higher wavenumbers.

## 4. Synthetic turbulence satisfying a prescribed energy spectrum

In the previous section, the relations among the shape function $f(r)$, the velocity spectrum tensor $\Phi_{ij}(\boldsymbol{\kappa})$ and the probability distribution $p(\lambda)$ in the CMSSEM are investigated. In this section, we apply those relations for the generation of HIT confirming to a prescribed energy spectrum $E(\kappa)$. To demonstrate the merits of the multi-scale feature in the CMSSEM, this job is done in two different approaches. In the first approach, we let $p(\lambda) = \delta(\lambda - 1)$ and determine the corresponding shape function according to eq. (2.46). In the second approach, we specify the shape function in prior and then determine $p(\lambda)$ from eq. (2.43). Thus, the eddies in these two approaches are of single-scale and multi-scale, respectively.

### *4.1. A model spectrum for real turbulence*

For practical purpose, we consider a energy spectrum model proposed by Stephen B. Pope [16], i.e.,

$$E(\kappa) = C\epsilon^{2/3}\kappa^{-5/3}f_L(\kappa L)f_\eta(\kappa\eta), \tag{4.1}$$

where $L$ is a length characterizing the scale of turbulence, $\epsilon$ is the energy dissipation rate, $\eta = (\nu^3/\epsilon)^{-1/4}$ is the Kolmogorov length scale and $\nu$ is the kinematic viscosity. The notation $f_L$ and $f_\eta$ stand for two non-dimensional functions and can be respectively taken as

$$f_L(\kappa L) = \left[\frac{\kappa L}{\left(c_L+\kappa^2L^2\right)^{1/2}}\right]^{5/3+p_0}, \tag{4.2a}$$

$$f_\eta(\kappa\eta) = \exp\left(-\beta\kappa\eta\right), \quad \beta = \left[2C\cdot\Gamma(\frac{4}{3})\right]^{4/3}, \tag{4.2b}$$

where $c_L$ and $p_0$ are positive constants. The function $f_L$, which determines the shape of $E(\kappa)$ in the energy-containing range, tends to unity for large $\kappa L$. Meanwhile, the function $f_\eta$, which controls the shape of $E(\kappa)$ in the dissipation rage, tends to unity for small $\kappa\eta$. In the inertial sub-range, both two functions approach to unity such that eq. (4.1) recovers to the Kolmogorov spectrum [17], i.e.,

$$E(\kappa) = C\epsilon^{2/3}\kappa^{-5/3}. \tag{4.3}$$

Without loss of generality, we set $p_0 = 4$ and $c_L = 1$. As a result, the model spectrum eq. (4.1) reduces to the von Kármán spectrum [18], i.e.,

$$E(\kappa) = C\epsilon^{2/3}L^{5/3}\frac{\kappa^4 L^4}{(1+\kappa^2 L^2)^{17/6}}, \tag{4.4}$$

for the wavenumber range in which $f_\eta \approx 1$. One can easily verify that by setting

$$C = \frac{55}{9\sqrt{\pi}}\frac{\Gamma(5/6)}{\Gamma(1/3)}, \tag{4.5}$$

the turbulence satisfying the von Kármán spectrum has isotropic variance of $\tau = \epsilon^{2/3}L^{2/3}$. Inserting eq. (4.4) into eq. (2.3), the length scale parameter $L$ in the von Kármán spectrum and the integral length scale $l$ of HIT can be shown to satisfy

$$\frac{l}{L} = \frac{\Gamma(5/6)}{\Gamma(1/3)}\sqrt{\pi}. \tag{4.6}$$

It is noted that the notation $L$ in this subsection is actually different from the earlier introduced eddy-scale parameter $L$ of the CMSSEM. However, we will set $L$ in the CMSSEM equal to the value of $L$ in the model spectrum eq. (4.1) in the following applications. It should also be noted again that the von Kármán spectrum is only valid in the energy-containing range and the inertial sub-range. In the dissipation range, the energy spectrum function should decay more rapidly than any power of $\kappa$, due to the fact that the velocity field is infinitely differentiable [16]. Hence, an exponential decay model such as eq. (4.2b) or the Pau spectrum [19] is more appropriate in the dissipation range.

### *4.2. Synthetic turbulence using single-scale eddies*

For energy spectrum functions as complicated as eq. (4.1), it is difficult to derive a shape function through eq. (2.46) analytically. Here, an alternative approach, in which eq. (2.46) is approximately satisfied, is presented. To do so, we first derive the shape function corresponding to the model spectrum with $f_\eta = 1$ (such that eq. (4.1) becomes the von Kármán spectrum). Inserting eq. (4.4) into eq. (2.46) and using $\gamma = \epsilon^{2/3}L^{2/3}$, this yields a shape function, denoted by $f_{\text{von}}(r)$, in the form of

$$f_{\text{von}}(r) = \frac{1}{2^{17/12}\Gamma(17/12)}\sqrt{\frac{C}{\pi}}\frac{K_{-1/12}(r)}{r^{1/12}}. \tag{4.7}$$

eq. (4.7) is not differentiable at $r = 0$ since $\lim_{r\to 0} f_{\text{von}}(r) = \infty$. This indicates that the eddies using a shape function of the form eq. (4.7) cannot generate a continuous local velocity distribution.

We then derive the shape function corresponding to the model spectrum with $f_L = 1$, in this case eq. (4.1) can be be reduced to

$$E(\kappa) = C\epsilon^{2/3}\kappa^{-5/3}f_\eta(\kappa\eta). \tag{4.8}$$

Inserting the above equation into eq. (2.46) and using eq. (4.2b), we obtain another shape function, denoted by $f_{\text{exp}}(r)$, which writes

$$f_{\text{exp}}(r) = -\sqrt{\frac{C}{2\pi^2}}\Gamma\left(-\frac{5}{6}\right)r^{-1}\left[\left(\frac{\beta\eta}{2}\right)^2 + r^2\right]^{5/12}\sin\left[\frac{5}{6}\text{atan}\left(\frac{2r}{\beta\eta}\right)\right]. \tag{4.9}$$

Compared to eq. (4.7), eq. (4.9) is differentiable everywhere in its domain and satisfies $f'_{\text{exp}}(0) = 0$. Using eqs. (4.7) and (4.9), we introduce a hybrid shape function for the model spectrum eq. (4.1) as

$$f_{\text{hybrid}}(r) = \begin{cases} f_{\text{exp}}(r) + f_{\text{von}}(r_0) - f_{\text{exp}}(r_0) & r \le r_0, \\ f_{\text{von}}(r) & r > r_0, \end{cases} \tag{4.10}$$

where $r_0$ is the location at which the first-order derivatives of $f_{\text{exp}}(r)$ and $f_{\text{von}}(r)$ are equal, i.e.,

$$\frac{\mathrm{d}}{\mathrm{d}} f_{\text{exp}}(r_0) = \frac{\mathrm{d}}{\mathrm{d}} f_{\text{von}}(r_0). \tag{4.11}$$

eq. (4.11) ensures that the continuity of the synthetic velocity field generated by the eddies with a shape function of the form eq. (4.10).

In fig. 2, the shape function eq. (4.10), its derivative and corresponding energy spectrum function for the case in which $L = 0.2\text{m}$, $\epsilon = 0.1581\text{m}^2/\text{s}^{-3}$ and $\eta = 3.8233 \times 10^{-4}\text{m}$ are demonstrated. Unless specifically specified, the von Kármán and model spectra considered in this section will all be computed using these parameters. Since it is difficult to derive the analytic expression for the Fourier transform of the shape function eq. (4.10), we estimate its resulting $E(\kappa)$ numerically using the Fast Fourier Transform (FFT) technique. The shape of the von Kármán and model spectra are also included in the plot for comparison. An excellent agreement between the targeted model spectrum and the theoretical energy spectrum function corresponding to the proposed shape function eq. (4.10) is noted.

We then generate a time-history of the turbulent velocity field on a two-dimensional plane of the dimension $2L \times 2L$, using the CMSSEM with $f_{\text{hybrid}}(r)$ for the shape function and $\delta(\lambda - 1)$ for $p(\lambda)$. It is assumed that the considered plane is normal to the $x_1$-direction and the mean velocity $\langle \boldsymbol{U} \rangle$ is aligned with this direction. A non-dimensional time-step size of $U\Delta t/L = 0.025$ (where $U$ denotes the magnitude of $\langle \boldsymbol{U} \rangle$) is employed and the turbulent velocity field is generated for a total of $1 \times 10^5$ time-steps. Other related parameters used in the synthesis of turbulence are listed in Table 3. The streamwise component (i.e., $u_1$) of the turbulent velocity at a specific point is shown in fig. 5a, which is filled up with exceedingly large peaks and doesn't look like real turbulence.

Finally, let's examine the spatial correlation of the synthetic turbulence and without loss of generality the one-dimensional spectrum of $u_1$ in the $x_1$-direction, denoted by $E_{11}^{(1)}(\kappa_1)$, is selected for consideration. Since the synthetic turbulence obeys Taylor's frozen turbulence hypothesis, we have its two-point correlation tensor satisfying

$$R_{ij}(r_1, 0, 0) = \langle u_i(\boldsymbol{x}, t) u_j(\boldsymbol{x}, t + r_1/U) \rangle, \tag{4.12}$$

where the right hand side of the above equality happens to be the two-time correlation tensor of the synthetic velocity. Using eq. (4.12), $E_{11}^{(1)}(\kappa_1)$ can then be obtained via the FFT of the time-history of $u_1$. Here, an overlapped segment averaging technique is adopted to obtain a smoothed spectrum and also to examine how the desired statistics concerning the synthetic turbulence converge with time. More specifically, the total time-history of $u_1$ is divided into a sequence of segments. Each segment contains the velocity sample for 2048 time-steps and the two adjacent segments share 50% overlap, resulting in a total of 96 segments for the time-step number of $1 \times 10^5$. We then compute $E_{11}^{(1)}(\kappa_1)$ from the FFT of each velocity segment and average the resulting spectra afterwards. fig. 6a plots the obtained spectrum averaged over all velocity segments, which shares an excellent comparison with the analytic expression of $E_{11}^{(1)}(\kappa_1)$ derived from

$$E_{11}^{(1)}(\kappa_1) = \int_{\kappa_1}^{\infty} \frac{E(\kappa)}{\kappa} \left(1 - \frac{\kappa_1^2}{\kappa^2}\right) \mathrm{d}\kappa. \tag{4.13}$$

To see how the $E_{11}^{(1)}(\kappa_1)$ of the synthetic turbulence converges to eq. (4.13) with the number of segments (denoted by $n$) used for averaging, we compute and plot in fig. 6b an error estimate given here

$$\Delta E_{11}^{(1)}(n) = \frac{1}{\langle u_1^2 \rangle} \int_0^{\kappa_{1,\max}} \left| \frac{1}{n} \sum_{i=1}^{n} E_{11,i}^{(1)}(\kappa_1) - E_{11}^{(1)}(\kappa_1) \right| \mathrm{d}\kappa_1 \tag{4.14}$$

where $E_{11,i}^{(1)}(\kappa)$ represents the spectrum obtained from the $i$-th segment of the total time-history of $u_1$, $E_{11}^{(1)}(\kappa_1)$ is desired spectrum given by eq. (4.13) and the upper integral limit $\kappa_{1,\max}$ is taken as $40\pi/L$ (considering more than 99% percent of the energy in contained below this wavenumber limit). The results in the plot indicate that the convergence of the introduced error estimate, for the present single-scale approach, slows down noticeably after $n = 40$, which corresponds to a dimensionless time instant $Ut/L$ of approximately 1000.

Table 3: Parameters employed for generating HIT satisfying the model spectrum on a two-dimensional plane of the dimension $2L \times 2L$ using the CMSSEM.

| Case | $L$ (m) | $\epsilon$ (m$^2$/s$^{-3}$) | $\eta$ (m) | $p(\lambda)$ | $f(r)$ | $\xi$ | $N$ |
|---|---|---|---|---|---|---|---|
| single-scale eddies | 0.2 | 0.1581 | $3.8233 \times 10^{-4}$ | $\delta(\lambda-1)$ | $f_{\text{hybrid}}$ | 3 | 2000 |
| multi-scale eddies | | | | $p_{\text{model}}$ | $f_{\text{gauss}}$ | | |

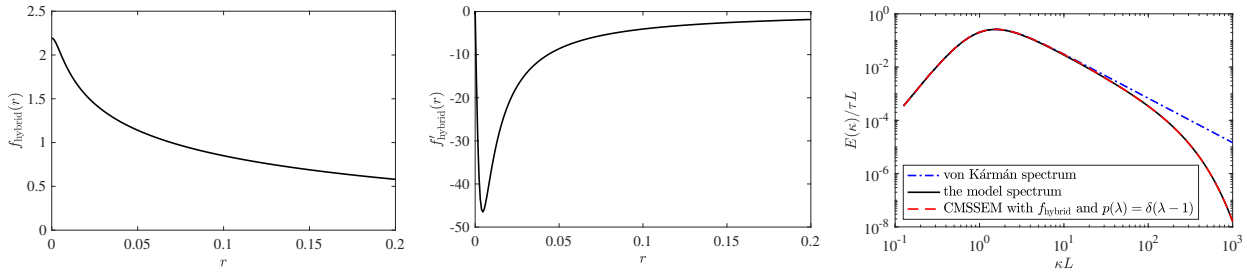


(a) $f_{\text{hybrid}}(r)$ (b) $f'_{\text{hybrid}}(r)$ (c) comparison of $E(\kappa)$

Figure 2: The shape function $f_{\text{hybrid}}(r)$, its derivative and resulting energy spectrum for the CMSSEM with $p(\lambda) = \delta(\lambda - 1)$.

### *4.3. Synthetic turbulence using multi-scale eddies*

Now, we apply the standard CMSSEM for the generation of HIT satisfying the model spectrum and employ the Gauss function (denoted by $f_{\text{gauss}}$) listed in Table 1 as the shape function. From eq. (2.43), the resulting energy spectrum function has the form of

$$E(\kappa) = \frac{4\tau L^5 \kappa^4}{\pi^3} \int_{\lambda_{\min}}^{\lambda_{\max}} \lambda^5 \exp\left(-\frac{\lambda^2 L^2 \kappa^2}{\pi}\right) p(\lambda)\, \mathrm{d}\lambda. \tag{4.15}$$

Unfortunately, it seems very challenging to derive an analytic expression for $p(\lambda)$, which can lead to reproducing the considered model spectrum exactly. However, it is noted that, when the random variable $\lambda$ of the eddies satisfies a probability distribution of the form

$$p_{\text{von}}(\lambda) = \frac{2}{\pi^{1/3}\Gamma(1/3)} \lambda^{-1/3} \exp\left(-\frac{\lambda^2}{\pi}\right), \tag{4.16}$$

with $\lambda_{\min} = 0$ and $\lambda_{\max} = \infty$, the corresponding energy spectrum function (determined by eq. (4.15)) coincides with the von Kármán spectrum exactly. One can easily verify that $p_{\text{von}}(\lambda)$ satisfy

$$\int_0^\infty p_{\text{von}}(\lambda) = 1, \quad \int_0^\infty \lambda p_{\text{von}}(\lambda) = \frac{\Gamma(5/6)}{\Gamma(1/3)}\sqrt{\pi}. \tag{4.17}$$

It can also be noticed that $p_{\text{von}}(\lambda)$ is infinity large at $\lambda = 0$ which violates the physical conception of eddies. We surmise that this happens because the von Kármán spectrum is not valid in the dissipation range in which $E(\kappa)$ should decay more rapidly than any power of $\kappa$. In practice, we can synthesize HIT satisfying the von Kármán spectrum approximately by employing a truncated function of $p_{\text{von}}(\lambda)$, i.e.,

$$\bar{p}_{\text{von}}(\lambda) = \begin{cases} C_p p_{\text{von}}(\lambda) & \lambda_{\min} \le \lambda \le \lambda_{\max}, \\ 0 & \lambda < \lambda_{\min} \text{ or } \lambda > \lambda_{\max}, \end{cases} \tag{4.18}$$

where $C_p$ is a normalization factor ensuring eq. (2.7). fig. 3 demonstrates the energy spectrum that can be reproduced by the CMSSEM using $\bar{p}_{\text{von}}(\lambda)$ with $\lambda_{\max} = 5$ and different values for $\lambda_{\min}$. As demonstrated in the plot, when a smaller value is assigned to $\lambda_{\min}$, the resulting $E(\kappa)$ can match with the von Kármán spectrum up to a higher wavenumber. This happens because the eddies with scales smaller than $\lambda_{\min} L$ are neglected when using $\bar{p}_{\text{von}}(\lambda)$ and those eddies have considerable contribution to the $E(\kappa)$ in the lager wavenumber region.

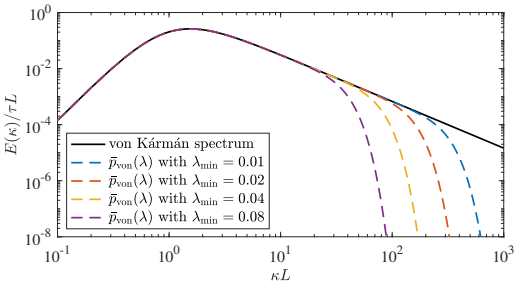


Figure 3: The energy spectrum theoretically reproduced by the CMSSEM using $f_{\rm gauss}(r)$ and $\bar{p}_{\rm von}(\lambda)$ with $\lambda_{\rm max} = 5$ and different values for $\lambda_{\rm min}$.

To acquire a probability distribution for $\lambda$, with which the model spectrum can be well reproduced, we consider a $p(\lambda)$ of the form

$$p_{\rm model}(\lambda) = \begin{cases} C_p p_{\rm von}(\lambda) \exp\left(-C_\lambda \lambda^{-\alpha_\lambda}\right) & \lambda_{\rm min} \le \lambda \le \lambda_{\rm max}, \\ 0 & \lambda < \lambda_{\rm min} \text{ or } \lambda > \lambda_{\rm max}. \end{cases} \tag{4.19}$$

where $\alpha_\lambda \ge 1$ and $C_\lambda$ are two constant parameters to be determined. The exponential term on the right hand side of eq. (4.19) is introduced here to make sure that $p_{\rm model}(\lambda) \approx p_{\rm von}(\lambda)$ when $\lambda$ is sufficiently large. For the determination of the $\lambda_{\rm min}$, $\lambda_{\rm max}$, $\alpha_\lambda$ and $C_\lambda$ in $p_{\rm model}(\lambda)$, we define the error between the energy spectrum function $E(\kappa)$ of the synthetic turbulence and the desired one $E_0(\kappa)$ over a specific wavenumber range of interest (namely $[0, \kappa_{\rm max}]$) as

$$e(\lambda_{\rm min}, \lambda_{\rm max}, \alpha_\lambda, C_\lambda) = \int_0^{\kappa_{\rm max}} |E(\kappa) - E_0(\kappa)| \, {\rm d}\kappa, \tag{4.20}$$

where $E(\kappa)$ is given by eq. (4.15). Thus, the determination of the four parameters in $p_{\rm model}(\lambda)$ can be regarded as an optimization problem in which eq. (4.20) is sought to be minimized. Using a general nonlinear optimization technique with $\kappa_{\rm max} L$ set to $10^3$, we obtain $\lambda_{\rm min} = 0.0075$, $\lambda_{\rm max} = 5.0$, $C_\lambda = 0.018$ and $\alpha_\lambda = 1.0$. fig. 4 demonstrates the $p_{\rm model}(\lambda)$ corresponding to these parameters and the resulting energy spectrum function. Similar to the former approach, the $E(\kappa)$ reproduced by the standard CMSSEM agrees excellently well with the targeted model spectrum. Again, we generate a time-history of the turbulent velocity field on the same two-dimensional plane as that of the previous subsection, using the shape function $f_{\rm gauss}$ and the probability distribution $p_{\rm model}(\lambda)$. For comparison purpose, we also employ the identical values for parameters $\xi$ and $N$. Note that, when using the same number of eddies, the computational effort required by the use of $f_{\rm gauss}$ as the shape function is much lower than that of $f_{\rm hybrid}$, since the evaluation of the Bessel function in the derivative of $f_{\rm hybrid}$ is way more computationally expensive.

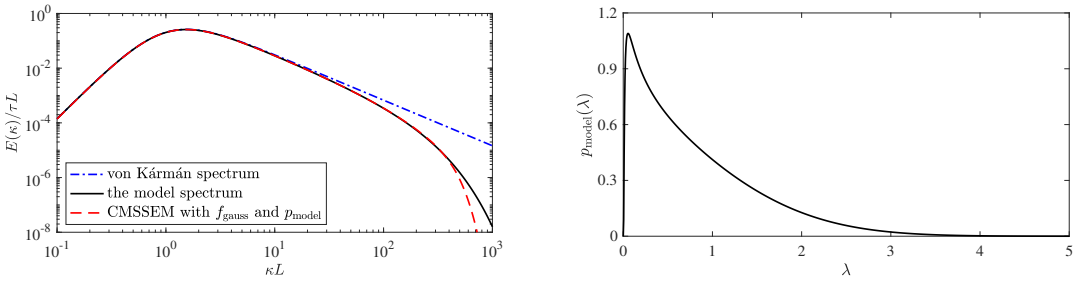


(a) comparison of $E(\kappa)$

(b) $p_{\rm model}(\lambda)$ optimized for the target spectrum

Figure 4: The energy spectrum theoretically reproduced by the CMSSEM and the optimized $p_{\rm model}(\lambda)$ employed for the reproduction of the model spectrum.

fig. 5b demonstrates the time-history of the synthetic turbulent velocity field at a specific point. Although the former single-scale approach and the present multi-scale approach both employ the same number of eddies, the time-histories of the turbulent velocity given by the two approaches look quite different. The velocity fluctuations obtained from the former approach (fig. 5a) look more spiky, while, those of the present approach (fig. 5b) seem smoothed. We also investigate the effect of the face-averaging operation (discussed early in section 3.4) on the synthetic turbulence in this example. fig. 5c plots the time-history of the face-averaged streamwise velocity computed with eq. (3.12) on a $x_1$-normal square face of the dimension $0.05L \times 0.05L$. The center of this square face coincides with the point considered in fig. 5b such that the effect of the face-averaging operation can be easily examined by comparing figs. 5b and 5c. It can be easily seen that the small-scale velocity fluctuations in fig. 5b are extensively averaged out in fig. 5c.

The spectrum $E_{11}^{(1)}(\kappa_1)$ of the synthetic velocity resulting from the present multi-scale approach, as well as that of the face-averaged synthetic velocity, are computed and shown in fig. 6a, using the aforementioned overlapped segment averaging technique. The spectrum of the original synthetic velocity has an excellent agreement with the desired spectrum similar to the single-scale approach, while, the effect of the face-averaging operation on suppressing the velocity fluctuations of smaller scales can be clearly seen from the velocity spectrum of the face-averaged synthetic velocity in the energy dissipation range.

The relation between the error estimate eq. (4.14) and the segment number, for the present multi-scale approach, is plotted in fig. 6b, which indicates that the obtained spectrum converges to the desired one a little faster than the single-scale approach. Also note that one efficient way to further accelerate the convergence of the statistics of the synthetic velocity is to increase the number of eddies. Recall the evaluation of the shape function $f_{\text{gauss}}$ in the multi-scale approach is way less computationally demanding than the shape function $f_{\text{hybrid}}$ in the single-scale approach. Thus, given the same computational time, the multi-scale approach may require even less time for averaging, compared to the single-scale approach, to obtain the desired statistics of turbulence.

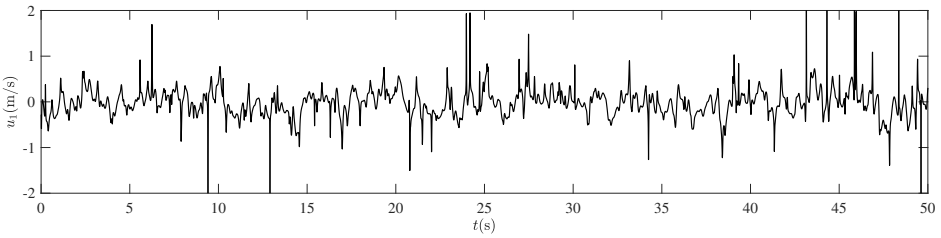


(a) $f_{\text{hybrid}}(r)$ and $p(\lambda) = \delta(\lambda - 1)$ (single-scale eddies)

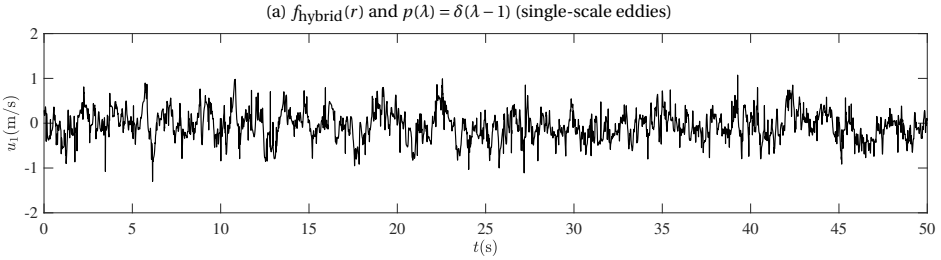


(b) $f_{\text{gauss}}(r)$ and $p_{\text{model}}(\lambda)$ (multi-scale eddies)

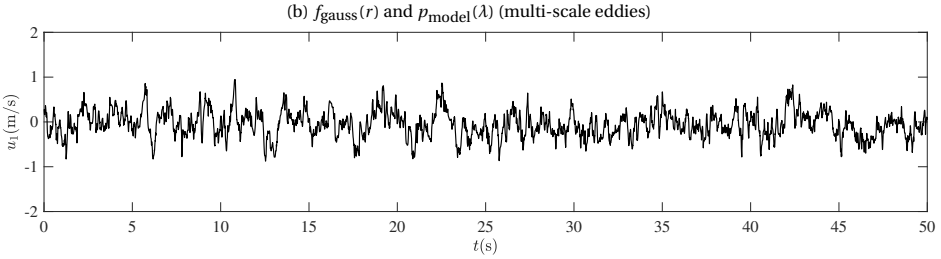


(c) face-averaged $f_{\text{gauss}}(r)$ and $p_{\text{model}}(\lambda)$ (multi-scale eddies)

Figure 5: The streamwise component of the turbulent velocities generated by the CMSSEM using single-scale and multi-scale eddies respectively (the target spectrum is the model spectrum).

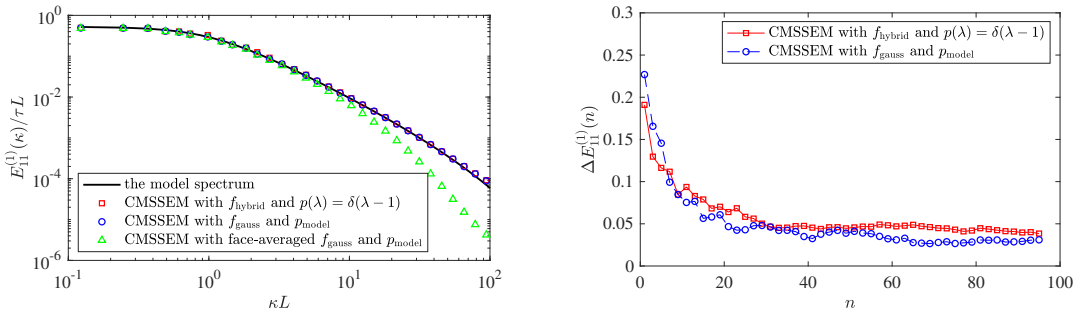


(a) the one-dimensional spectrum $E_{11}^{(1)}(\kappa)$

(b) convergence of the error estimate $\Delta E_{11}^{(1)}(n)$

Figure 6: The one-dimensional spectrum $E_{11}^{(1)}(\kappa)$ and its error estimate $\Delta E_{11}^{(1)}(n)$ of the turbulent velocities generated by the CMSSEM for the reproduction of the model spectrum using single-scale and multi-scale eddies respectively (the target spectrum is the model spectrum).

### *4.4. Further comments the two approaches*

Finally, we'd like to further comment on what contributes to the distinct difference between the synthetic turbulence given by the single-scale and the multi-scale approaches. When both of these are respectively employed to reproduce the same energy spectrum, the shape function employed in the single-scale approach can be viewed as a function summing up the contribution of a set of pseudo eddies whose scales range over $[\lambda_{\min}L, \lambda_{\max}L]$. This set of pseudo eddies, which formulate the single-scale eddy in the former approach, can be regarded to share an identical spatial location and assigned to a universal sign parameter. As a result, the shape function of this single-scale eddy is characterized by two features: a sharp peak at the eddy-center region and a flat decaying slope at the region far from the eddy-center (see fig. 2a for reference). Shape functions like this apparently make the synthetic turbulence unrealistic. In comparison, the standard multi-scale approach seeks avoids this issue by breaking up the single-scale eddy into multiple ones with varying positions, scales and different sign parameters. As shown in the presented example, the length scale of multi-scale eddies varies over a considerable broad range, where the largest scale can be ten or hundred times of the smallest scale. Given a sufficiently large amount of synthetic eddies, the overlapping among them (or more specifically their bounding boxes) should be very common, which results in the random fluctuations of various scales and amplitudes in the synthetic velocity. This happens to be the essential feature that makes the synthetic turbulence of the multi-scale approach more realistic than that of the single-scale approach.

## 5. Numerical example

To further examine the performance of the CMSSEM for the generation of real turbulence, we apply it the reproduction of the grid-generated HIT experimentally studied by [20]. The energy spectrum (see fig. 7), identified from the turbulence at $U_0 t/M = 42$ downstream a grid with the mesh size of $M = 0.0508$m (where $U_0 = 10$m/s is the upstream air speed approaching the grid), is selected for consideration. To reproduce such an energy spectrum, we keep using the Gauss-type shape function and employing $p_{\text{model}}(\lambda)$ for the probability distribution of the eddy scales. The four parameters in $p_{\text{model}}(\lambda)$ as well as the length scale parameter $L$ of the CMSSEM are still determined by minimizing eq. (4.20). After a general nonlinear optimization, we obtain $L = 0.03$m, $\lambda_{\min} = 0.06$, $\lambda_{\max} = 5.07$, $C_\lambda = 2.03 \times 10^{-5}$ and $\alpha_\lambda = 1.96$. A comparison of the spectrum corresponding to this set of parameters with the experimentally identified spectrum is shown in fig. 7.

Next, we apply the optimized $p_{\text{model}}(\lambda)$ for the generation of a turbulent velocity field which is periodic in the three axial directions. The turbulent velocity field is respectively generated on three orthogonal collocated finite volume grid systems all with a dimension of $(1/5\pi, 1/5\pi, 1/5\pi)$m (approximately 12 times of the grid mesh-size $M$ in each dimension), resulting a minimum wavenumber of $\kappa_0 = 10\text{m}^{-1}$. The three grid systems have 32, 64 and 128 uniformly distributed nodes in each direction, respectively. We use a total of 4096 eddies for the synthesis of turbulence and the synthetic turbulent velocity fields on the three grid systems employ the same set of eddies. The cell-face velocity of the finite volume grid is computed as the face-averaged synthetic velocity, as suggested in

section 3.4, to satisfy the spatially-discretized continuity equation exactly. The cell-center velocity of the finite volume grid is computed as the cell-volume-averaged synthetic velocity to cope with the large eddy simulation (LES) technique which will be used later. Similar to the face-averaged synthetic velocity, there also exists an analytic expression for the volume-averaged synthetic velocity attained by a Gauss-type shape function, which is omitted here for simplicity.

Due to the periodicity of the synthetic velocity field, the energy spectrum function is now computed with

$$E(\kappa, t) = \frac{1}{2} \sum_{\kappa-1/2<|\boldsymbol{\kappa}|<\kappa+1/2} |\hat{u}_{\boldsymbol{\kappa}}|^2, \tag{5.1}$$

where $\kappa \in \mathbb{N}^+$ and $\hat{u}_{\boldsymbol{\kappa}}$ is the $\boldsymbol{\kappa}$-th Fourier coefficient of the synthetic cell-center velocity at the time instant $t$. The energy spectra of the synthetic velocity fields on the three grids are demonstrated in fig. 9a, respectively. It can be easily seen that the energy spectrum identified on the finer grid can better match the targeted one including a larger wavenumber range. A noteworthy factor accounts for this finding is the volume-averaging operation applied to the synthetic velocity at cell-centers, the influence of which on related second-order statistics gets weaker for smaller grid spacing.

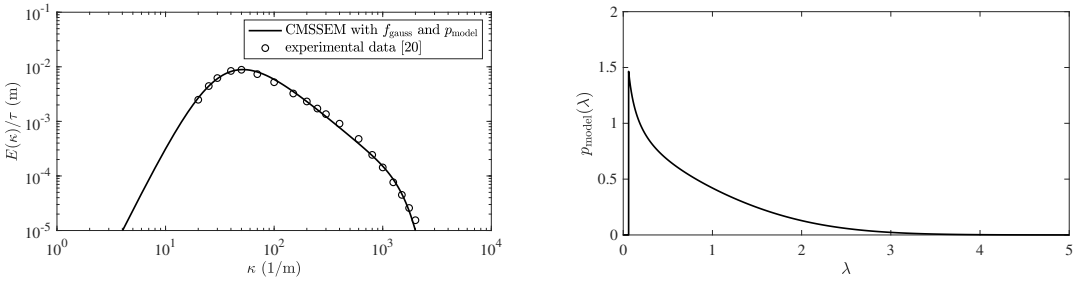


(a) comparison of $E(\kappa)$

(b) the optimized $p_{\text{model}}(\lambda)$

Figure 7: The energy spectrum theoretically reproduced by the CMSSEM and the optimized $p_{\text{model}}(\lambda)$ employed for the reproduction of the energy spectrum identified from the experiment of [20].

Finally, we simulate the decay of the synthetic turbulent velocity field on the time-internal $U_0 t/M \in [42, 171]$ for the three grids respectively using LES. The numerical simulation is conducted using a standard transient solver for incompressible turbulent flow, i.e., pimpleFoam, provided in the OpenFOAM v2206. The eddy viscosity SGS model proposed by [21] is employed for the subgrid modeling of LES. The dimensionless time-step size $U_0 \Delta t/M$ is taken as 0.3937, 0.1969 and 0.0984 for the three grid systems respectively, which ensures that the maximum Courant numbers under different cases are roughly the same.

After the numerical simulation of the synthetic velocity field, we first compare the decay of its turbulent kinetic energy to the empirical curve identified from the measurement of [20] in fig. 8. Logarithmic scales are used in the plot so that curve appears as a straight line if the turbulent kinetic energy decays exponentially with time. It is easy to see the turbulent kinetic energy of the synthetic velocity field at the initial time-instant (i.e., $U_0 t/M = 42$) is noticeably lower than its desired value also due to the volume-averaging operation. We also find the decaying curves of the turbulent kinetic energy, for all of the three considered grids, differ from the experimental measurement quite a lot at the beginning of the simulation. It is only after around $U_0 t/M = 100$ that they appear as a straight line with an slope closed to the measurement. Apart from the errors in the numerical simulation itself, a main factor that could account for this finding is that there are still some underlying differences between the synthetic turbulence generated by the CMSSEM and the targeted real turbulence although their second-order statistics are almost identical. As a result, when the synthetic turbulence is employed as the initial condition of the simulation, it takes some evolution time for the simulated flow field to recover the characteristics and flow patterns of real turbulence.

The energy spectra of the turbulent velocity fields developed in the numerical simulation at $U_0 t/M = 98$ and 171 are computed and compared with the experimental data provided in [20], see fig. 9. Good agreements, especially for the two finer grids, can be noted in these plots, which highlights the performance of the CMSSEM in

the reproduction of the desired energy spectrum. We also demonstrate the correlation functions of $u_1$ in the $x_1$- and $x_2$-directions, i.e., $R_{11}(r_1,0,0)$ and $R_{11}(0,r_2,0)$, from the numerical and experimental data in figs. 10 and 11. The variances of $u_1$ at the considered time-instants from the experimental measurement are used to normalize the corresponding correlation functions. For most of the spectra and correlation functions shown in the plots, the numerical and experimental data demonstrate a better agreement at $U_0 t/M = 42$ and 171 (i.e., the beginning and the end of the simulation) compared to $U_0 t/M = 98$. This confirms our finding on the decay of the turbulent kinetic energy in numerical simulations, which again indicates that a developing time period is needed for the synthetic turbulence to get closer to real turbulence.

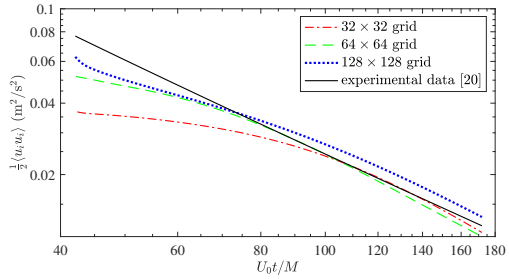


Figure 8: Time evolution of the kinetic energy $k = \frac{1}{2}\langle u_i u_i \rangle$ of the decaying turbulence initially synthesized by the CMSSEM on different grids.

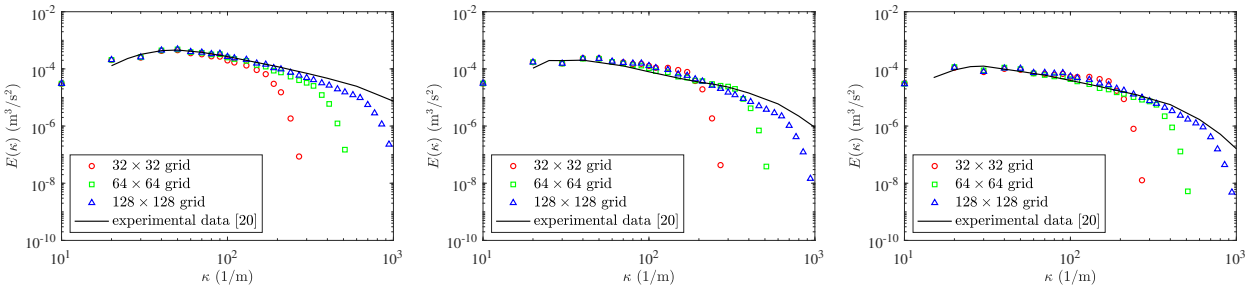


(a) $U_0 t/M = 42$ (the initial time-instant) (b) $U_0 t/M = 98$ (c) $U_0 t/M = 171$

Figure 9: The energy spectrum $E(\kappa)$ of the decaying turbulence initially synthesized by the CMSSEM at selected time-instants.

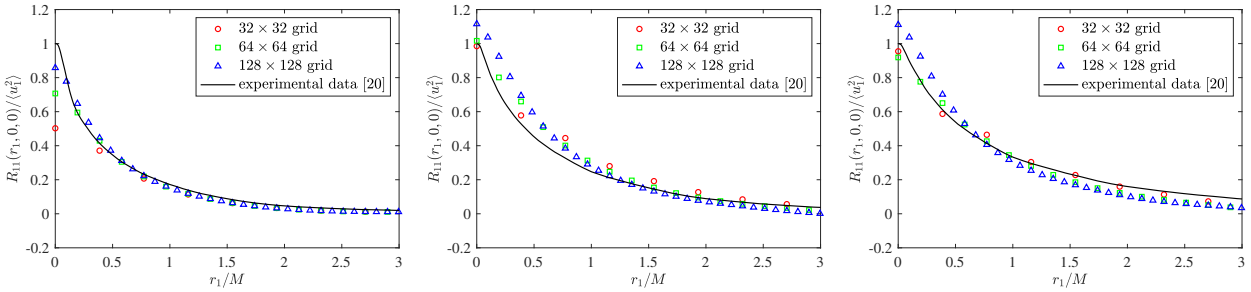


(a) $U_0 t/M = 42$ (the initial time-instant) (b) $U_0 t/M = 98$ (c) $U_0 t/M = 171$

Figure 10: The correlation function $R_{11}(r_1,0,0)$ of the decaying turbulence initially synthesized by the CMSSEM at selected time-instants.

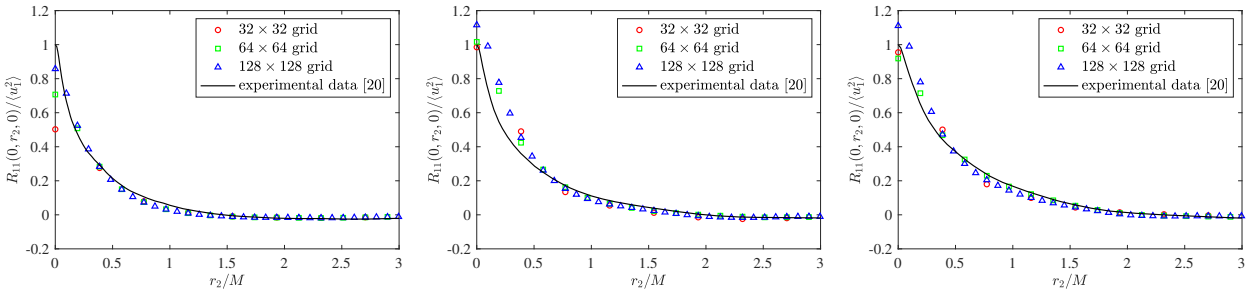


(a) $U_0 t/M = 42$ (the initial time-instant) (b) $U_0 t/M = 98$ (c) $U_0 t/M = 171$

Figure 11: The correlation function $R_{11}(0, r_2, 0)$ of the decaying turbulence initially synthesized by the CMSSEM at selected time-instants.

## 6. Concluding remarks

In this study, a new divergence-free synthetic eddy method is developed for the generation of HIT confirming to a prescribed energy spectrum. The proposed SEM is characterized by a multi-scale feature in which each synthetic eddy is assigned to a unique length scale determined by a dimensionless random variable $\lambda$ satisfying a particular probability distribution $p(\lambda)$. Considering the length scales of the eddies vary continuously over a fixed interval, we name the proposed method as the continuous multi-scale synthetic eddy method or the CMSSEM in abbreviation.

In the CMSSEM, the divergence-free constraint is enforced by computing the turbulent velocity field as the curl of a synthetic vector potential field following conventional approach. The vector potential carried by each synthetic eddy is computed from a shape function which takes the Euclidean distance from a spatial location to the center of the eddy divided by the scale of the eddy as its argument. By analyzing the second-order statistics of the synthetic turbulence, it is shown that the CMSSEM is capable of reproducing the energy spectrum tensor of incompressible HIT exactly.

The mathematical relation, i.e., eq. (2.43), concerning the energy spectrum function of the synthetic turbulence, the shape function of the eddies and $p(\lambda)$, is derived analytically. When the shape function is explicitly specified, the equality can be considered as a Fredholm integral equation of the first kind regarding the unknown $p(\lambda)$. In practice, we can also approximate the solution of $p(\lambda)$ by expressing it as a basic function with some unknown parameters. The unknown parameters are optimized by minimizing the difference between the energy spectrum function of the synthetic turbulence and the targeted spectrum.

We also discuss an issue which has seldom been addressed in previous studies on divergence-free SEM methodology, that is, making the synthetic velocity field satisfy the spatially-discretized continuity equation exactly. Taking the finite volume grid as an example, this requirement can be be easily satisfied by computing the velocity at a cell-face center as the face-averaged synthetic velocity, as long as there exists an analytic expression for the computation of such a quantity.

For performance validation, the CMSSEM is first applied to the generation of HIT satisfying an energy spectrum model of real turbulence. To demonstrate the merits of the multi-scale feature in the CMSSEM, the synthesis of turbulence is conducted using eddies of single-scale and multi-scale, respectively. For the single-scale eddy case, the employed shape function is derived from the considered energy spectrum according to the relation of eq. (2.43) with $p(\lambda) = \delta(\lambda - 1)$. For the multi-scale eddy case, we employ a Gauss-type shape function and propose a model function for $p(\lambda)$, i.e., $p_{\text{model}}$. Note that $p_{\text{model}}$ is adapted from another probability distribution $p_{\text{von}}$, which can be used for synthesizing HIT satisfying the von Kármán spectrum exactly. While two cases show excellent results in reproducing the targeted spectrum with the same number of eddies, the multi-scale case requires less computational effort and generates a more realistic turbulence. The effects of the face-averaging operation on the synthetic turbulence and its energy spectrum are also examined for the multi-scale eddy case. It tends to flatten the velocity fluctuations caused by smaller scales eddies at the cost of suppressing the magnitude of the energy spectrum at larger wavenumbers.

The CMSSEM is further tested by synthesizing a grid-generated turbulent velocity field identified from wind tunnel experiments. In this example, we further simulate the decay of the synthetic turbulence in time-domain

using the finite volume method and the LES technique, and compare the resulting time-varying energy spectrum with the experimental data. The use of multi-scale synthetic eddies with the Gauss-type shape function allows us to compute the cell-center (or cell-face) velocity of the finite volume grid as the volume-averaged (or face-averaged) synthetic velocity easily. The CMSSEM again attains satisfactory performance in this example.

Finally, it should be addressed again that this study only concerns HIT. The CMSSEM can be easily adaptable to anisotropic homogeneous turbulence by introducing multiple length scale and intensity parameters to synthetic eddies, details of which will be presented in our future work.

### CRediT authorship contribution statement

**Yunzhu Cai**: Conceptualization, Writing – original draft. **Jiawei Wan**: Methodology, Code development and numerical experiments. **Ahsan Kareem**: Revised the manuscript, Supervision.

### Declaration of competing interest

The authors declare that they have no known competing financial interests or personal relationships that could have appeared to influence the work reported in this paper.

### Data availability

The code and data related to the figures, tables and numerical examples in this study are available in the Code Ocean, at https://doi.org/10.24433/CO.5923657.v3.

### Acknowledgments

The authors gratefully acknowledge the support provided in part by the NSF Grant Nos. 1612843 & 2131111 and the Natural Science Research of Jiangsu Higher Education Institutions of China Grant No. 22KJB560004.

### References

[1] N. Jarrin, S. Benhamadouche, D. Laurence, and R. Prosser. A synthetic-eddy-method for generating inflow conditions for large-eddy simulations. *International Journal of Heat and Fluid Flow*, 27(4):585–593, 2006.

[2] N. Kornev and E. Hassel. Method of random spots for generation of synthetic inhomogeneous turbulent fields with prescribed autocorrelation functions. *Communications in Numerical Methods in Engineering*, 23(1):35–43.

[3] Nicolas Jarrin. *Synthetic inflow boundary conditions for the numerical simulation of turbulence.* A thesis submitted to the University of Manchester for the degree of doctor of philosophy in the faculty of engineering and physical sciences, 2008.

[4] Nikolai Kornev and Egon Hassel. Synthesis of homogeneous anisotropic divergence-free turbulent fields with prescribed second-order statistics by vortex dipoles. *Physics of Fluids*, 19(6):068101, 2007.

[5] R. Poletto, T. Craft, and A. Revell. A new divergence free synthetic eddy method for the reproduction of inlet flow conditions for les. *Flow, Turbulence and Combustion*, 91:519–539, 2013.

[6] Hannes Kröger and Nikolai Kornev. Generation of divergence free synthetic inflow turbulence with arbitrary anisotropy. *Computers & Fluids*, 165:78–88, 2018.

[7] Adrian Sescu and Ray Hixon. Toward low-noise synthetic turbulent inflow conditions for aeroacoustic calculations. *International Journal for Numerical Methods in Fluids*, 73(12):1001–1010, 2013.

[8] Robert H. Kraichnan. Diffusion by a random velocity field. *The Physics of Fluids*, 13(1):22–31, 1970.

[9] Jakob Mann. Wind field simulation. *Probabilistic Engineering Mechanics*, 13(4):269–282, 1998.

[10] Tony Saad, Derek Cline, Rob Stoll, and James C. Sutherland. Scalable tools for generating synthetic isotropic turbulence with arbitrary spectra. *AIAA Journal*, 55(1):327–331, 2017.

[11] Jae Wook Kim and Sina Haeri. An advanced synthetic eddy method for the computation of aerofoil–turbulence interaction noise. *Journal of Computational Physics*, 287:1–17, 2015.

[12] Yin Luo, Hongjun Liu, Qin Huang, Huili Xue, and Kun Lin. A multi-scale synthetic eddy method for generating inflow data for LES. *Computers & Fluids*, 156:103–112, 2017.

[13] G. K. Batchelor. *The Theory of Homogeneous Turbulence.* Cambridge University Press, 1953.

[14] G. I. Taylor. The spectrum of turbulence. *Proceedings of the Royal Society of London. Series A - Mathematical and Physical Sciences*, 164(919):476–490, 1938.

[15] Harry Hochstadt. *Integral Equations.* John Wiley & Sons, Ltd, 1988.

[16] Stephen B. Pope. *Turbulent Flows*. Cambridge University Press, 2000.
[17] Kolmogorov, A., and N. The local structure of turbulence in incompressible viscous fluid for very large reynolds numbers. *Proceedings of the Royal Society A: Mathematical*, 434(1890):9–13, 1991.
[18] Theodore Von Karman. Progress in the statistical theory of turbulence. *Proceedings of the National Academy of Sciences of the United States of America*, 34(11):530, 1948.
[19] Yih-Ho Pao. Structure of turbulent velocity and scalar fields at large wavenumbers. *The Physics of Fluids*, 8(6):1063–1075, 1965.
[20] Genevieve Comte-Bellot and Stanley Corrsin. Simple eulerian time correlation of full-and narrow-band velocity signals in grid-generated isotropic turbulence. *Journal of Fluid Mechanics*, 48(2):273–337, 1971.
[21] Akira Yoshizawa. Statistical theory for compressible turbulent shear flows, with the application to subgrid modeling. *The Physics of Fluids*, 29(7):2152–2164, 1986.